

Evidence for a Cool Disk and Inhomogeneous Coronae from Wide-band Temporal Spectroscopy of Cygnus X-1 with Suzaku

Shin'ya YAMADA¹, Kazuo MAKISHIMA^{2,1,4}, Chris DONE³, Shunsuke TORII², Hirofumi NODA², and Soki SAKURAI²

¹ *Cosmic Radiation Laboratory, Institute of Physical and Chemical Research (RIKEN),*

2-1 Hirosawa, Wako-shi, Saitama, 351-0198

² *Department of Physics, University of Tokyo, 7-3-1, Hongo, Bunkyo-ku, Tokyo 113-0033*

³ *Department of Physics, Durham University, South Road, Durham, DH1 3LE, UK*

⁴ *Research Center for the Early Universe, RESCEU, University of Tokyo, 7-3-1, Hongo, Bunkyo-ku, Tokyo 113-0033*

yamada@crab.riken.jp

(Received 2012, December, 12; accepted 2013, April, 2)

Abstract

Unified X-ray spectral and timing studies of Cygnus X-1 in the low/hard and hard intermediate state were conducted in a model-independent manner, using broadband Suzaku data acquired on 25 occasions from 2005 to 2009 with a total exposure of ~ 450 ks. The unabsorbed 0.1–500 keV source luminosity changed over 0.8–2.8% of the Eddington limit for 14.8 solar masses. Variations on short (1–2 seconds) and long (days to months) time scales require at least three separate components: a constant component localized below ~ 2 keV, a broad soft one dominating in the 2–10 keV range, and a hard one mostly seen in 10–300 keV range. In view of the truncated disk/hot inner flow picture, these are respectively interpreted as emission from the truncated cool disk, a soft Compton component, and a hard Compton component. Long-term spectral evolution can be produced by the constant disk increasing in temperature and luminosity as the truncation radius decreases. The soft Compton component likewise increases, but the hard Compton does not, so that the spectrum in the hard intermediate state is dominated by the soft Compton component; on the other hand, the hard Compton component dominates the spectrum in the dim low/hard state, probably associated with a variable soft emission providing seed photons for the Comptonization.

Key words: black hole physics – accretion – stars: individual (Cygnus X-1) – X-ray:binaries

1. Introduction

X-rays have been an essential probe to study energetic astrophysical phenomena, including mass accretion onto black holes in particular. Starting with the first identification of Cygnus X-1 (hereafter Cyg X-1) as a black hole binary in the early 1970's (e.g., Oda et al. 1971, Tananbaum et al. 1972, Thorne & Price 1975), the spectral as well as timing studies of black hole binaries, including Cyg X-1, have established the presence of two distinct states: the high/soft state and the low/hard state (e.g., Remillard & McClintock 2006, Done et al. 2007).

In the high/soft state, an optically thick and geometrically thin accretion disk (Shakura & Sunyaev 1973) releases most of the gravitational energy in locally thermal equilibrium radiation. The spectra in this state can be fairly well reproduced by multi-color blackbody radiation (Mitsuda et al. 1984 and Makishima et al. 1986) from such a “standard” accretion disk and a powerlaw emission with a photon index of ~ 2.5 of which the origin is commonly considered to be Compton scattering by a disk corona with a hybrid (thermal + non-thermal) electron distribution (e.g., Dotani et al. 1997, Gierliński et al. 1999, and Gou et al. 2011), along with reflection features arising from disk regions illuminated by the powerlaw component. A typical high/soft state spectrum from Cyg X-1 is shown

as black in figure 1.

In the low/hard state, the spectrum is no longer dominated by the disk emission. Instead, most of the energy is released in hard X-rays via un-saturated Comptonization by Maxwellian electrons (e.g., Sunyaev & Trümper 1979). This Comptonizing region, conventionally called a “corona”, is hot (with a typical temperature of ~ 100 keV, possibly with a much higher ion temperature, so most probably geometrically thick), and optically thin, in marked contrast to the standard disk which is cool, geometrically thin and optically thick. However, some optically thick material is still present in this state: there is a weak thermal component seen in the soft X-ray bandpass which presumably provides seed photons for the Comptonization, and there is clear evidence for some reflected emission (iron lines and Compton humps; e.g., Gierliński et al 1997; Gilfanov, Churazov & Revnivtsev 1999; Di Salvo et al. 2001, Zdziarski & Gierliński 2004, Ibragimov et al 2005). A typical low/hard state spectrum from Cyg X-1, highlighting the very different properties of this state, is shown in red in figure 1.

The relative geometry of the disk and corona in the low/hard state is still a matter of debate. One type of models assume that the corona replaces the inner disk, with the flow making a transition to an alternative, hot, geometrically thick, optically thin solution to the accre-

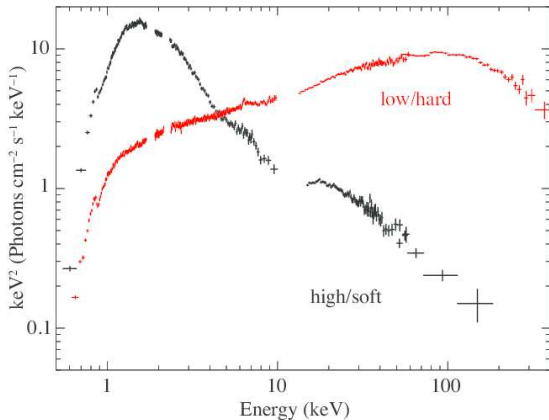


Fig. 1. Suzaku spectra of Cyg X-1 in the response-removed νF_ν form. The black one was obtained in the high/soft state on 2010 December 16. The red one was taken in the low/hard state on 2005 October 5, which is the same as used in Makishima et al. (2008).

tion flow equations (e.g., Shapiro et al. 1976; Ichimaru 1977; Narayan & Yi 1995). Exterior to this, the outer truncated disk provides a source of seed photons for the Compton scattering from the hot flow, and a site for the reflected emission. These truncated disk/hot inner flow models are successful in explaining the clear correlations seen in the data (e.g. Gilfanov, Churazov & Revnivtsev 1999; Zdziarski & Gierliński 2004, Done, Gierliński & Kubota 2007). Alternatively, other geometries have also been proposed, the vertically separated sandwich “disk-corona configuration” (e.g., Liang & Price 1977, Haardt et al. 1991, Poutanen et al. 1993), the vertically offset “lamppost” model (e.g. Fabian et al 2012), and the vertically outflowing corona (Beloborodov et al. 1999).

A key difference between these models for the low/hard state is the location of the innermost disk radius. In the truncated disk model, it is assumed to be larger than the innermost stable circular orbit, while in the other geometries the disk is envisaged to extend down to the last stable orbit. However, a number of spectral analyses (e.g., Gierliński et al. 1997; Zdziarski et al. 1998; Frontera et al. 2001) and timing studies (Miyamoto & Kitamoto 1989; Negoro et al. 1994; Nowak et al. 1999; Gilfanov et al. 2000; Revnivtsev et al. 1999; Remillard & McClintock 2006) were unable to unambiguously settle the issue. This is because the disk emission is much weaker than the Comptonized emission in this state, appearing only as a very subtle excess in the lowest energies as shown in figure 1. To constrain the disk emission requires the best possible constraints on the broad band Comptonized emission.

Suzaku, the fifth Japanese X-ray satellite, carries the X-ray Imaging Spectrometer (XIS; Koyama et al. 2007) located at the foci of the X-ray Telescope (XRT; Serlemitsos et al. 2007), and a non-imaging hard X-ray instrument, the Hard X-ray Detector (HXD; Takahashi et al. 2007; Kokubun et al. 2007; Yamada et al. 2011). These two instruments enable us to simultaneously measure a wide-

band (typically 0.5–300 keV) spectrum of bright hard X-ray sources. With this capability, Suzaku has observed Cyg X-1 25 times from 2005 to 2009 in the low/hard state and hard intermediated state, over which the 1–10 keV flux varied by a factor of ~ 3 . The 0.5–300 keV spectra taken in the first observation has been reproduced by Makishima et al. 2008 (Paper I), invoking two (hard and soft) Comptonization components, a truncated disk, and reflection components (the “double-Compton modeling” itself was first applied to Cyg X-1 by Frontera et al. 2001 and to AGN by Magdziarz et al. 1998). Based on the “double-Compton modeling” and other observational facts as to Fe-K lines and the reflection strength, they proposed that there is an overlapping region between the disk and corona, and changes in the coronal coverage fraction of the disk produce the fast variation. Although this view was confirmed in subsequent Suzaku observations (Nowak et al. 2011, Fabian et al 2012), these authors discussed several possible alternatives to the double-Compton view, including non-thermal Comptonization, jet emission, and complex ionized reflection.

To disentangle such modeling degeneracy, we use the variability on different timescales and try to identify separate spectral components in a model-independent way. This was already initiated by Torii et al. 2011 (Paper II), who analyzed the HXD (PIN and GSO) data from the 25 observations for spectral and timing properties of the hard X-ray emission. At that time, they were not able to include the XIS data as these are often severely affected by photon pileup. Because of this limited energy range, they could fit their data by a single Comptonization component together with a simple reflection model. Now that we have established a method to correct XIS data for pile-up effects (Yamada et al. 2012), we can complement the work in Paper II, by including all the 25 XIS data sets.

Thus in this paper, we can use the entire broad band-pass of Suzaku to study the spectral evolution through the low/hard and hard-intermediate state.

The distance to Cyg X-1 has been recently determined as $D = 1.86^{+0.12}_{-0.11}$ kpc, via a trigonometric parallax measurement using Very Long Baseline Array (Reid et al. 2011). This value is consistent with an independent measurement using dust scattering halo (Xiang et al. 2011). Based on this distance, the black hole mass and its inclination were derived as $14.8 \pm 1.0 M_\odot$ and $27.1 \pm 0.8^\circ$ (Orosz et al. 2011), respectively. We adopt these values throughout the present paper. Unless otherwise stated, errors refer to 90% confidence limits.

2. Observation and Data reduction

2.1. Observations

Like Paper II, the present paper deals with the 25 Suzaku data sets of Cyg X-1, of which basic information is listed in table 1. The grey points in figure 2a presents the long term count-rate and hardness-ratio histories of Cyg X-1 from the RXTE All Sky Monitor (ASM) public data. The ASM count rates for the Suzaku observation period are estimated from the ASM daily count rates and

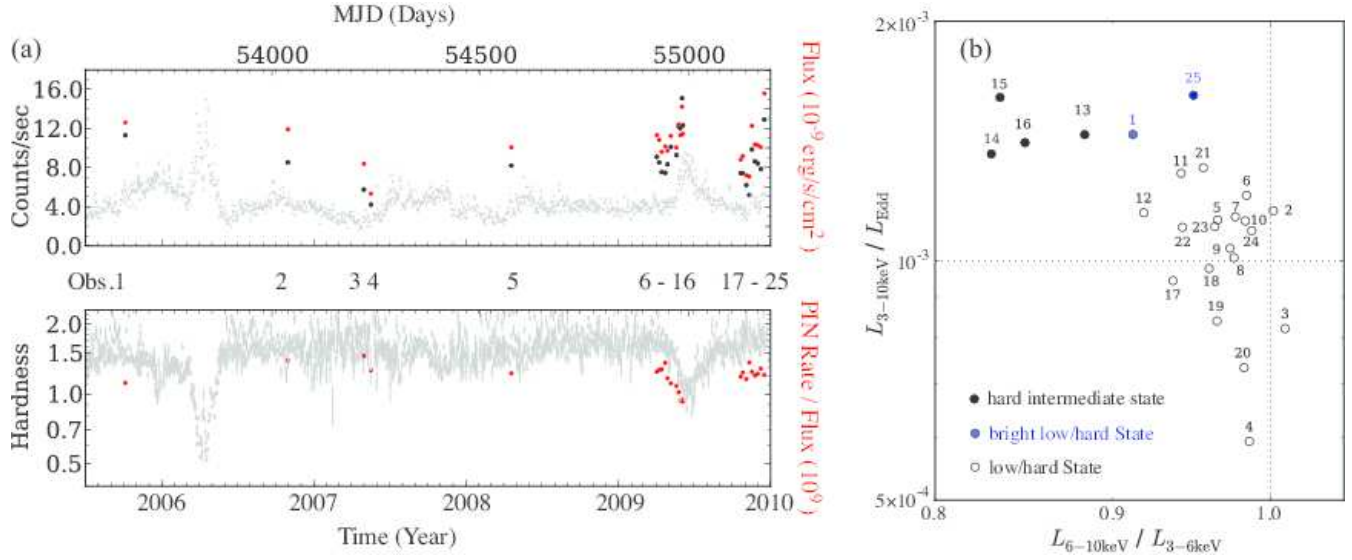


Fig. 2. (a) The 1.5–12 keV count-rate history of Cyg X-1 (gray), taken with the RXTE/ASM from 2005 July to 2010 January, which are scaled down to 25%. The 0.5–10 keV flux of the XIS and the 15–20 keV count rate of PIN are superposed in red and black, respectively. The bottom panel shows the hardness ratios of the 15–20 keV count rates of PIN to the 0.5–10 keV XIS fluxes ($\times 10^9$) (red dots), superposed on the 5–12 keV to 1.5–3 keV hardness of the ASM (gray). (b) The 6–10 keV to 3–6 keV hardness ratio of the XIS plotted against the 3–10 keV intensity derived from the XIS normalized by the Eddington luminosity. All data are not corrected for the absorption.

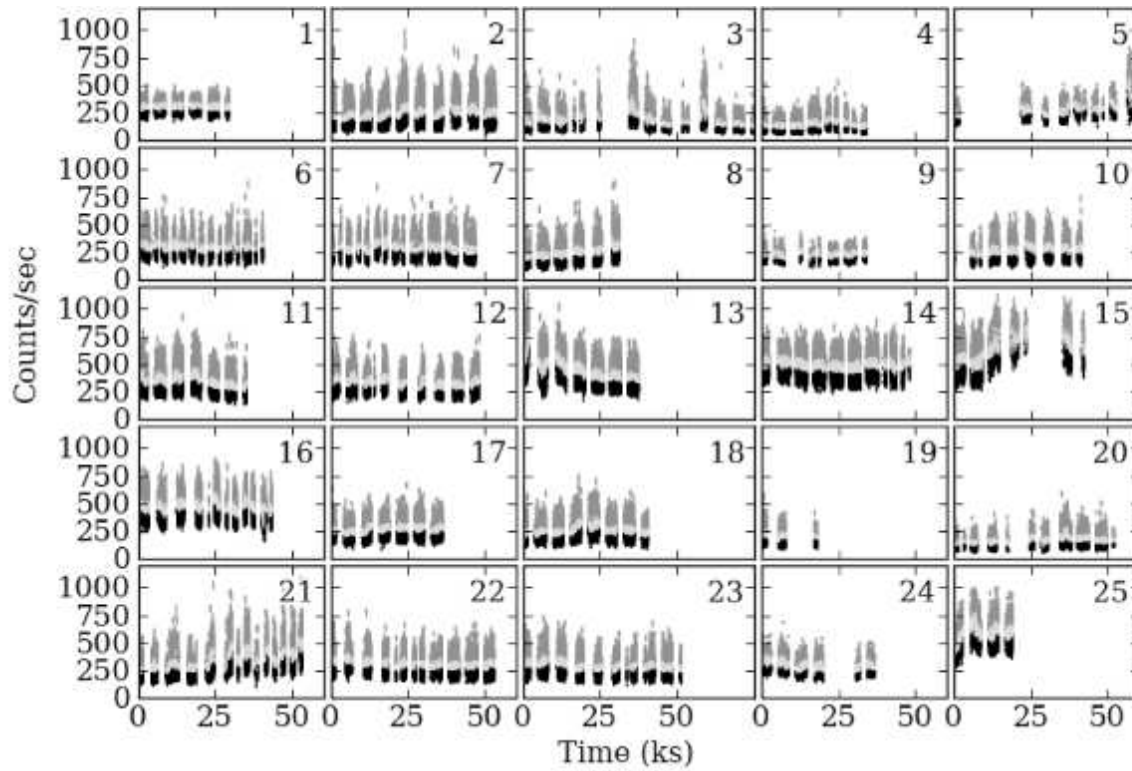


Fig. 3. The 0.5–10 keV XIS3 light curves of Cyg X-1 for the 25 observations. The bin size is set at 1.0 s for 1/8 window options (Obs. 1 and 2) and timing mode (Obs. 5, 9, 24, and 25), while 2.0 s for the others. The data during dipping periods are removed. High-, intermediate-, and low-flux phases are shown in dark gray, light gray, and black, respectively.

Table 1. The log of Suzaku observations of Cyg X-1 taken from 2005 to 2009.

N	Date (UT)	T [†] (ks)	Nom.*	Obs. ID	ASM*	Hard*	Orb. Phase [‡]	$F_{0.5-10}^{\S}$	$L_{0.1-500}/L_{\text{Edd}}^{\parallel}$
1	2005-10-05T04:51:39	37.2	XIS	100036010	29.0	1.41	0.563–0.640	11.3	2.80(1.70)
2	2006-10-30T03:36:11	58.1	HXD	401059010	21.2	1.41	0.199–0.319	8.5	1.83(1.56)
3	2007-04-30T19:35:34	83.6	HXD	402072010	12.9	1.82	0.819–0.992	5.7	1.28(1.18)
4	2007-05-17T19:41:23	71.5	HXD	402072020	14.0	1.59	0.856–0.003	4.2	0.85(0.77)
5	2008-04-18T16:21:38	64.1	HXD	403065010	17.2	2.00	0.011–0.144	8.2	1.57(1.36)
6	2009-04-03T01:17:23	44.2	HXD	404075010	22.0	1.54	0.401–0.492	9.1	1.87(1.52)
7	2009-04-08T06:09:03	48.9	HXD	404075020	21.7	1.61	0.330–0.431	8.5	1.70(1.45)
8	2009-04-14T18:21:40	33.0	HXD	404075030	19.7	1.54	0.492–0.561	7.5	1.53(1.29)
9	2009-04-23T04:01:10	39.6	HXD	404075040	20.0	1.54	0.993–0.075	7.4	1.53(1.36)
10	2009-04-28T17:02:23	43.9	HXD	404075050	22.6	1.39	0.983–0.073	8.3	1.58(1.36)
11	2009-05-06T16:48:59	37.6	HXD	404075060	21.0	1.61	0.410–0.487	10.1	1.85(1.45)
12	2009-05-20T00:34:56	50.1	HXD	404075080	23.9	1.12	0.789–0.892	9.3	1.63(1.23)
13	2009-05-25T08:35:49	40.4	HXD	404075090	31.8	1.05	0.741–0.825	12.2	2.00(1.44)
14	2009-05-29T11:53:46	48.6	HXD	404075100	33.7	1.12	0.480–0.581	12.0	1.97(1.22)
15	2009-06-02T11:33:13	43.7	HXD	404075110	45.0	1.05	0.192–0.282	15.9	2.28(1.43)
16	2009-06-04T19:42:00	44.5	HXD	404075120	35.0	1.12	0.610–0.702	12.3	2.05(1.29)
17	2009-10-21T09:03:11	40.0	HXD	404075130	18.9	1.43	0.353–0.435	7.4	1.40(1.11)
18	2009-10-26T06:21:56	41.7	HXD	404075140	18.9	1.59	0.226–0.312	7.4	1.41(1.20)
19	2009-11-03T21:28:15	44.6	HXD	404075150	14.0	1.69	0.767–0.859	6.2	1.70(0.98)
20	2009-11-10T19:39:56	53.4	HXD	404075160	17.4	1.89	0.003–0.114	5.1	1.05(0.98)
21	2009-11-17T06:51:08	56.7	HXD	404075170	24.4	1.75	0.158–0.275	9.8	1.81(1.56)
22	2009-11-24T12:20:29	53.5	HXD	404075180	22.4	1.59	0.449–0.559	8.6	1.63(1.33)
23	2009-12-01T07:00:50	51.7	HXD	404075190	25.0	1.61	0.659–0.766	8.4	1.65(1.36)
24	2009-12-08T15:32:11	39.5	HXD	404075200	22.2	1.75	0.973–0.054	7.8	1.56(1.38)
25	2009-12-17T01:29:11	42.2	HXD	404075070	40.9	1.59	0.475–0.563	12.9	2.28(1.87)

* “Nom” is the nominal pointing mode; “ASM” is the 1.5–12 keV count rate obtained with the RXTE All Sky Monitor; “Hard” is the hardness ratio of 5–12 keV to 1.5–3 keV ASM count rates.

† From the start to the end of the observation.

‡ Using the orbital period of 5.599829 days, with phase 0 (the epoch of a superior conjunction of the black hole) being MJD41874.207 (Brocksopp et al. 1999).

§ The absorbed flux in 0.5–10 keV in units of 10^{-9} erg s⁻¹ cm⁻².

|| The unabsorbed luminosity in 0.1–500 keV divided by L_{Edd} and absorbed ones in the parentheses

summarized in table 1. The red and black points in figure 2a (top) show the Suzaku data used in this paper, with 0.5–10 keV fluxes measured with the XIS (absorption is not corrected), $F_{0.5-10}$, and the 15–20 keV count rates in PIN, respectively. The hardness ratio of the 15–20 keV PIN count rate to the 0.5–10 keV fluxes ($\times 10^9$) are plotted in red points in figure 2a (bottom). The heterogeneous hardness ratio is used to compensate for the differences in count rates of XIS for different observation modes. Both the ASM and Suzaku data show an increase in the flux and a decrease in the hardness ratio in the middle of 2009.

Cyg X-1 is considered to be in the high/soft state when the ASM hardness ratio is $\lesssim 0.8$, according to the criterion Fender et al. (2006) proposed. Since all the present 25 observations have the hardness ratio > 0.8 , none of them can be classified as the high/soft state. The moderate softening observed in 2009 is regarded as a “failed transition”, wherein the source evolved from the low/hard state possibly to the hard intermediate state.

For a more detailed state identification, the 25 observations are arranged in a hardness-luminosity diagram in figure 2b. Following Dunn et al. (2010), we used the luminosity in 3–10 keV, $L_{3-10 \text{ keV}}$, divided by the Eddington luminosity, $L_{\text{Edd}} = 1.5 \times 10^{38} (14.8 M_{\odot} / M_{\odot})$ erg s⁻¹ given the hydrogen fraction of 0.7, and the hardness between 6–10 keV and 3–6 keV, $L_{6-10 \text{ keV}} / L_{3-6 \text{ keV}}$, where $L_{6-10 \text{ keV}}$ is the luminosity in 6–10 keV. Our data mostly sample the top of the low/hard state “stalk” on the hardness-intensity diagram, where the hardness stays approximately constant while the intensity increases. In figure 2b, several of the 25 data points, corresponding to the failed transition mentioned above, are seen to connect into the hard intermediate state, where the hardness decreases markedly for little increase in intensity (states as defined in Homan & Belloni 2005). Spectra at the top of the stalk (Obs. 1 and 25) can either be classified as bright low/hard state or as hard intermediate state. We classify them as hard intermediate state in the rest of this paper.

2.2. The XIS data

2.2.1. Processing of the XIS data

The operation modes of the XIS are summarized in table 2. Among the four XIS cameras, XIS2 was operational until Obs. 2., while it stopped working since 2006 November. To reduce piled-up events, the 1/8 or 1/4 window mode was employed, together with burst options (Koyama et al. 2007). One of the XIS data in Obs. 5, 9, 24, and 25 are taken in a timing mode, or Parallel(P)-sum mode, which is one of the clocking modes in the XIS.

We begin with the standard screening criteria of the XIS as follows: (1) the XIS Grade (Koyama et al. 2007) should be 0, 2, 3, 4, or 6, (2) the time interval after an exit from the South Atlantic Anomaly should be longer than 436 s, and (3) the object should be at least 5° and 20° above the dark and sunlit Earth rim, respectively. Data taken with the time mode were processed with a different Grade selection¹: Grade 0 (single event), as well as 1 and 2 (double events), were used. These data have a time resolution of 7.8 ms owing to onboard summation over one of the two dimensions.

Since Cyg X-1 is very bright and the combination of the XIS and the XRT provides a relatively broad spatial resolution of $\sim 2'$ in a half-power diameter (Serlemitsos et al. 2007), it is difficult to extract non X-ray background (NXB) from the outskirts of the XIS image. Therefore, we estimated the NXB level using the events acquired in a north-ecliptic pole region, dominated by the NXB (Kubota et al. 2010). The NXB was then found to contribute $\lesssim 0.1\%$ to the Cyg X-1 data even at the highest energy end, ~ 10 keV. Therefore, in the present XIS analysis, the NXB subtraction is not needed.

The source brightness instead demanded additional two screening steps: to exclude those periods when the telemetry of the XIS was saturated, and to avoid piled-up photons of the XIS. The former was discarded by using the house keeping data, `ae*xi*_tel_uf.gti`. The latter was practically realized by excluding a center region of the image, to minimize pileup effects at the sacrifice of photon statistics. This “core excision” method was calibrated for the XIS data analysis in data-oriented way (Yamada et al. 2012). We also corrected the XIS image for smearing effects due to thermal wobbling of the spacecraft (Uchiyama et al. 2008).

2.2.2. Lightcurves and spectra of the XIS

Since Cyg X-1 has a supergiant companion, the accreting gas is supplied by its strong stellar winds. This causes episodes of increased absorption, or “dips”, which are seen as decreases in soft X-rays at near the superior conjunction of the black hole (e.g., Kitamoto et al. 1984). Since we are interested in the intrinsic emission properties of Cyg X-1, these dipping periods were removed as detailed in Appendix 1.

We then extracted events from an annulus with the inner radius of $R_{3\%}$ as shown in table 5 in Appendix 2 and the outer radius of $4'$, where $R_{x\%}$ refers to the radii

¹ see http://www.astro.isas.ac.jp/suzaku/analysis/xis/psum_recipe/Psum-recipe-20100724.pdf

Table 2. Window/burst options applied to the XIS.

	XIS0	XIS1	XIS3
N^*	Mode	Mode	Mode
1 [†]	1/8W 1.0 s	1/8W 1.0 s	1/8W 1.0 s
2 [†]	1/8W 0.3 s	1/8W 0.3 s	1/8W 0.3 s
5	timing	std [‡]	std
9	timing	std	timing
24	std	std	timing
25	std	std	timing

* The observation number used in table 1.

† The modes and exposures of XIS2 are the same as those of XIS0.

‡ “std” means a standard mode for a bright source: 1/4 window mode and 0.5 s burst option. In the other 20 observations, the XIS cameras were all operated in “std”.

at which the pileup fraction is $x\%$. These details are described in Appendix 2. Since adopting much smaller pileup fractions (much stronger core excision) would increase systematic uncertainties in the XIS and XRT response (Yamada et al. 2012), the pileup fraction of 3% for spectral analysis is practically reasonable.

Figure 3 shows 0.5–10 keV light curves of XIS3 extracted from a circle with a radius of $4'$, since the count rate is less susceptible to pileup than spectral shape. In Obs. 5, 9, 24, and 25, either the XIS0 or XIS3 data acquired in the timing mode were used.

The response matrices and auxiliary response files were created with `xissimrmfgen` and `xissimarfgen`, respectively (Ishisaki et al. 2007); the latter properly takes into account areas used for spectral extraction, and the widow shapes of the XIS sensors. The systematic differences in normalization among the four (or three) XIS sensors are less than $\sim 3\%$ (suzakumemo 2008-06²).

2.3. The HXD data

2.3.1. Processing of the HXD data

The PIN and GSO events were screened by their standard criteria: the target elevation angle $\geq 5^\circ$, cutoff rigidity ≥ 6 GV, and 500 s after and 180 s before the South Atlantic Anomaly. The telemetry-saturated and FIFO-full periods (Kokubun et al. 2007) were discarded. In order to utilize the latest GSO calibration results (Yamada et al. 2011), we have reprocessed all the GSO data with `hxdpi` implemented in HEASoft 6.9 or later, together with the corresponding gain history parameter table, `ae*gpt*fits`.

The NXB of the HXD was subtracted from the raw data as described in Fukazawa et al. (2009). The cosmic X-ray background was not subtracted from either the PIN or GSO data, since its contribution integrated over the HXD filed of view is $< 0.1\%$ of the signal in any energy range.

² <http://www.astro.isas.ac.jp/suzaku/doc/suzakumemo/suzakumemo-2008-06.pdf>

The basic information on the HXD data is almost the same as that in Paper II, so that the details are summarized in Appendix 3.

2.3.2. Lightcurves and spectra of the HXD data

We used the responses of PIN and GSO provided by the detector team. The NXB of PIN was generally less than 1% of the source signals therein, and at most $\sim 10\%$ at ~ 60 keV. The NXB of GSO became comparable to the source signals at ~ 150 keV. Since systematic uncertainties in the NXB of GSO are at most $\sim 3\%$ (Fukazawa et al. 2009), we use the spectra up to ~ 300 keV. More detailed studies of the spectra and timing properties of the HXD data were reported in Paper II.

2.4. Correlations of fluxes in different energy bands

The left side panel in figure 4 presents the relation of the flux in 0.5–10 keV, $F_{0.5-10}$, to the count rates of the ASM, PIN and GSO, as well as the 10–200 keV flux. All of them show a positive correlation with $F_{0.5-10}$, which means that the overall source behavior, to the first approximation, is controlled by a single parameter; i.e., the spectrum normalization, which is considered to reflect the mass accretion rate. However, the spectral shape is also varying to some extent, since the 0.5–10 keV flux changes more than the 100–200 keV flux.

To better visualize these spectral changes, we show hardness ratios in the right hand panel of figure 4. When the 0.5–10 keV flux exceeds $\sim 7 \times 10^{-9}$ erg s $^{-1}$ cm $^{-2}$ (marking the top of the low/hard state “stalk” in the hardness-intensity diagram in figure 2b) the hardness ratio to all bands starts to decrease, and this effect increases towards higher energies, suggesting that not only a spectral slope steepens but also a high energy cutoff becomes lower.

2.5. Estimating the Eddington ratios

To assess the Eddington ratios for our sample, we employed the same double Comptonization model as used in Makishima et al. 2008 with the neutral column density fixed at 7×10^{21} cm $^{-2}$. Since the model reproduced the wide-band spectra within several percents, we evaluated absorbed and unabsorbed 0.1–500 keV fluxes by extrapolating the best-fit model spectra. Considering isotropic emission, we obtained absorbed and unabsorbed 0.1–500 keV luminosities, $L_{0.1-500}$, by multiplying obtained fluxes by $4\pi D^2$, and listed them in table 1. Our data sample a range of 0.8–2.8% of L_{Edd} , which are grossly typical values observed from black hole binaries in the low/hard state.

3. Long-term Spectral Analysis

3.1. Wide-Band Spectra

Removal of instrumental responses (conventionally “unfolding”) is useful to make spectral changes more directly visible, without being affected by the instrumental effects such as energy-dependent detector efficiencies. This is usually performed after finding the best-fit models, because results of deconvolution are known to depend on the employed model (so-called obliquing effect). However,

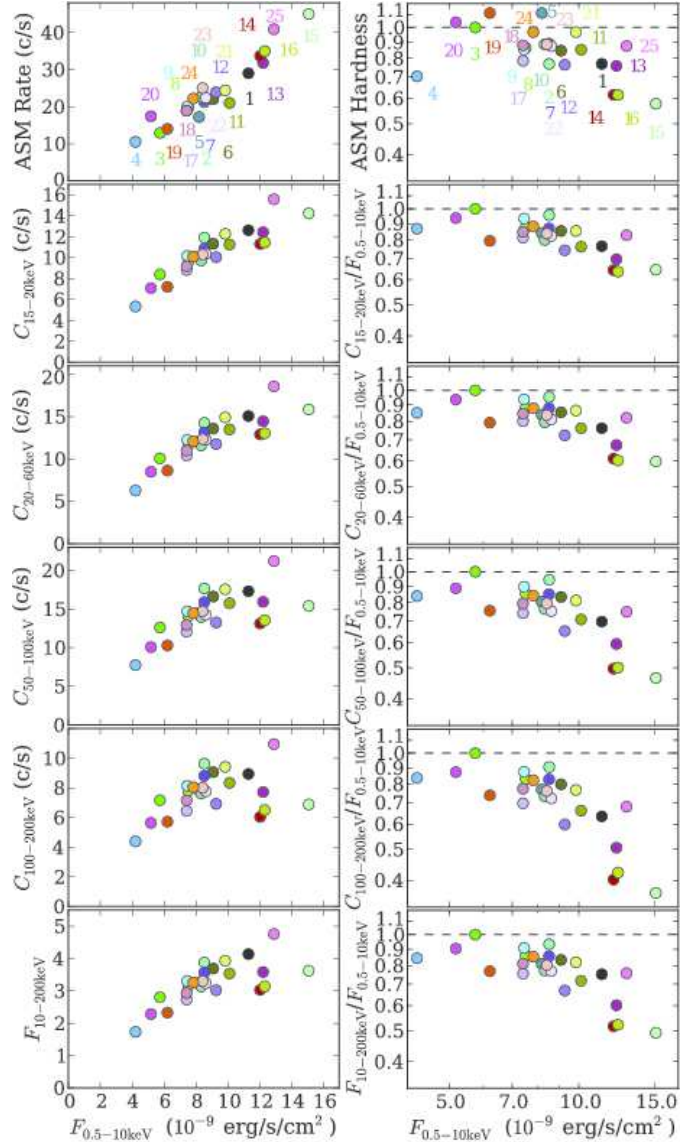


Fig. 4. (left; top to bottom) The 1.5–12 keV ASM count rate, the 15–20 keV PIN count rate, that in 20–60 keV, the 50–100 keV GSO count rate, that in 100–200 keV, and the 10–200 keV signal flux, all plotted against the 0.5–10 keV signal flux, $F_{0.5-10}$. The 25 observations are specified by colors. (right) Hardness ratios in various energy bands, all plotted against $F_{0.5-10}$. The top panel show the 5–12 keV to 1.5–3 keV ratios for the RXTE ASM, while the lower 5 panels give ratios of the count rates in the corresponding left-column panel to $F_{0.5-10}$. All are normalized to the value of Obs. 3.

this effect is considered negligible even if we use next-to-best fitting models, as long as the model and the data are both free from features which are comparable to or narrower than the instrumental energy resolution. Therefore, we try to find approximately good fitting models, and perform the deconvolution.

In fitting the broad-band spectra, we used the response and auxiliary files described in section 2.2.2 for the XIS and 2.3.2 for the HXD. The cross normalization between the XIS and HXD was fixed at the standard value of 1.17, of which the uncertainty is estimated to be less than $\sim 5\%$ based on the Crab Nebula data (suzakumemo 2008-06). Then, we fitted separately the XIS and HXD spectra with conventional models, `diskbb + powerlaw` and `compps`, respectively, where `diskbb` is a multicolor disk model (Mitsuda et al. 1984; Makishima et al. 1986) and `compps` is one of the Comptonization models valid for $\tau < 3$ (Poutanen & Svensson 1996). Using these models, we conducted the spectral deconvolution. The deconvolved spectra are changed by less than $< 1\%$ when these different models are used.

Figure 5 shows the deconvolved 0.5–300 keV spectra of the 25 Suzaku observations of Cyg X-1, presented in the $\nu F\nu$ form, and sorted in terms of decreasing soft X-ray flux ($F_{0.5-10}$ given in table 1). We overlay the hardest spectrum (Obs. 3) in grey on all the data. This visualizes systematic changes in the spectral shape as a function of $F_{0.5-10}$, which are suggested by the hardness ratios of figure 4. We also note that the four spectra on the top row in figure 5, with the highest $F_{0.5-10}$ flux, correspond to the hard intermediate state spectra of figure 2b, while the rest are in the low/hard state.

At a first glance, these $\nu F\nu$ spectra all show very similar shapes, monotonically rising up to ~ 100 keV, then sharply falling. This is especially true for all the low/hard state spectra. These results agree, at least qualitatively, with the previous Suzaku studies of Cyg X-1 conducted in the low/hard and hard-intermediate state (Obs. 1: Makishima et al. 2008; Obs. 1-4: Nowak et al. 2011; Obs. 7: Fabian et al. 2012).

By inspecting figure 5 more closely, we can deduce the following characteristics of the spectral changes which occurred among the observations on a time scale of days to months.

1. As the flux increases, the emission below ~ 10 keV becomes more prominent.
2. At the same time as 1, the 10–100 keV spectral slope steepens and the cutoff feature at ~ 100 keV moves to lower energies.
3. Contrary to 2, in the dimmest two observations, Obs. 20 and 4, the spectrum softens even though the flux decreases.

The last property is characteristic of dimmer low/hard state spectra from other black hole binaries (e.g. Sobolewska et al. 2011), but this is the first time it has been identified in Cyg X-1. The transition of “softer when brighter” into “harder when brighter” behavior in Cyg X-

1 appeared at $L_{\text{Edd}} \sim 0.01$, which agrees with the results of GRO J1655-40 and GX 339-4 studied by Sobolewska et al. 2011. Thus, it implies that some changes in accretion at $L_{\text{Edd}} \sim 0.01$ might be a universal property of black hole binaries.

3.2. Spectral Ratios on a Time Scale of $> \text{Days}$

To more directly examine the spectral differences among the observations, we created spectral ratios in figure 6, again using the hardest spectrum (Obs. 3) as a reference. The properties (1)–(3) noticed in subsection 3.1 are more clearly visualized. The ratios are larger than 1.0 for all data below 10 keV (apart from the two lowest luminosity spectra, Obs. 20 and 4), but is always larger at 1 keV than at 10 keV. Thus the long term variability is largest at soft energies.

This long term variability clearly has (at least) two components. For example, in Obs. 15 (the brightest hard intermediate state), the ratio shows a sharp upturn below 2 keV, then a steady decline in the 3–30 keV bandpass and a sharper decline above 100 keV. To zeroth order this is what is expected when the seed photons illuminating the Compton region increase by more than the power dissipated in the hot electrons (Zdziarski et al. 2002; Zdziarski & Gierliński 2005) as the photon index steepens, and electron temperature drops.

A further inspection of the $\nu F\nu$ spectrum of Obs. 15 in figure 5 shows that the spectral changes above 3 keV cannot be explained by considering the two components (disk and Comptonization) only. In brighter spectra, the ratio starts rising abruptly at 3–4 keV toward lower energies, where the disk emission should still be negligible. Therefore, the data indicate the presence of an additional soft continuum component with a spectral index of $\Gamma \sim 2$ which dominates below 10 keV.

4. Short-term Spectral Analysis

We first explore the rising component below 10 keV. If this contains the disk, then it can have very different variability properties from the corona. Hence we look at the rapid (1–2s) variability in the XIS, and use this to separate out the corona from the slower variability of the disk component.

4.1. Definition and preparation

We use “intensity-sorted spectroscopy”, as defined in Paper I to study the spectral variability on a time scale of 1–2 s. Specifically, we define high-flux phase as

$$\{t \mid C(t) > (1+f) \overline{C(t)}_T\}, \quad (1)$$

while low-flux phase as

$$\{t \mid C(t) \leq (1-f) \overline{C(t)}_T\}, \quad (2)$$

where $C(t)$ and t are the count rate and the event arriving time, respectively, f is a threshold to determine the high and low intensities, T is an interval over which $C(t)$ is averaged, and $\overline{C(t)}_T$ denotes the average count rate over the interval of $t - T/2 < t < t + T/2$. The gap between

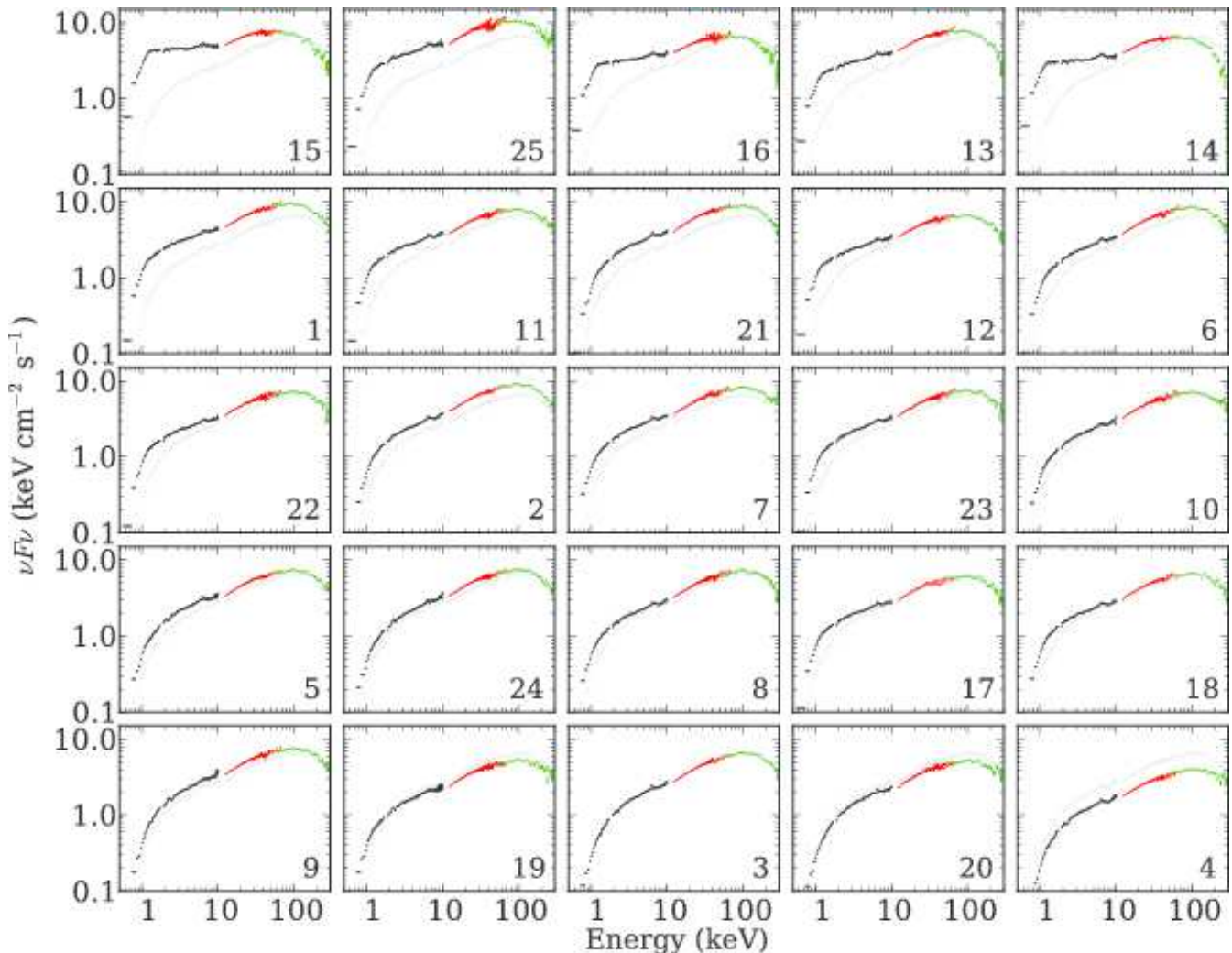


Fig. 5. Background-subtracted Suzaku spectra of Cyg X-1 from the 25 observations, shown in the νF_ν form after removing the detector responses. The spectra of XIS, PIN, and GSO are shown in black, red, and green, respectively. The XIS data refer to XIS3, except in Obs. 9 in which XIS1 is used, and Obs. 24 and 25 wherein XIS0 is employed. The spectra of Obs. 3 are superposed in light gray as a reference.

the high and low phases is defined as an intermediate-flux phase. This differs slightly from Paper I in that we calculate $\overline{C}(t)_T$ as a running average at every t , while in Paper I it was set every 200 seconds in a discrete manner.

When conducting the intensity-sorted spectroscopy with a single detector, we need to set f rather high to avoid Poisson noise; otherwise, the high and low spectra would pick up the effects of statistical fluctuations. However, in the present case, this problem can be avoided by judging the high and low phases using a detector, and accumulating the high and low spectra using the other detectors. Specifically, we make the lightcurve $C(t)$ from one of the XIS cameras, and determine the high/low flux phase based on equation (1) and (2). Then, according to the criteria, the high-phase and low-phase events of the other XIS cameras are obtained.

For creating $C(t)$, the 0.5–10 keV count rate of XIS3 was used after excluding the dipping periods. We set f at 0.05 as a compromise between photon statistics and

the contrast in intensity, and T at 64 s. The color coding on figure 3 gives the high (dark grey), intermediate (light grey), and low (black) phases determined for all observations according to these parameters.

4.2. Spectral changes on a time scale of 1–2 s

We first looked in detail at the low energy data. We sorted the XIS1 events into the high and low phases according to the criteria in section 4.1, and obtained the results shown in figure 7 in νF_ν form. To zeroth order, the low and high spectra exhibit similar shapes; i.e., the source variation on the 1–2 s time scale occurs primarily keeping the spectral shapes constant.

We then extend the energy band using the PIN and GSO data. We form the high and low spectra for each observation across the entire energy band and show the ratio of the high-phase spectrum to the low-phase one in figure 8. These ratio plots reveals more subtle variations. There is a clear peak in the variability at energies around

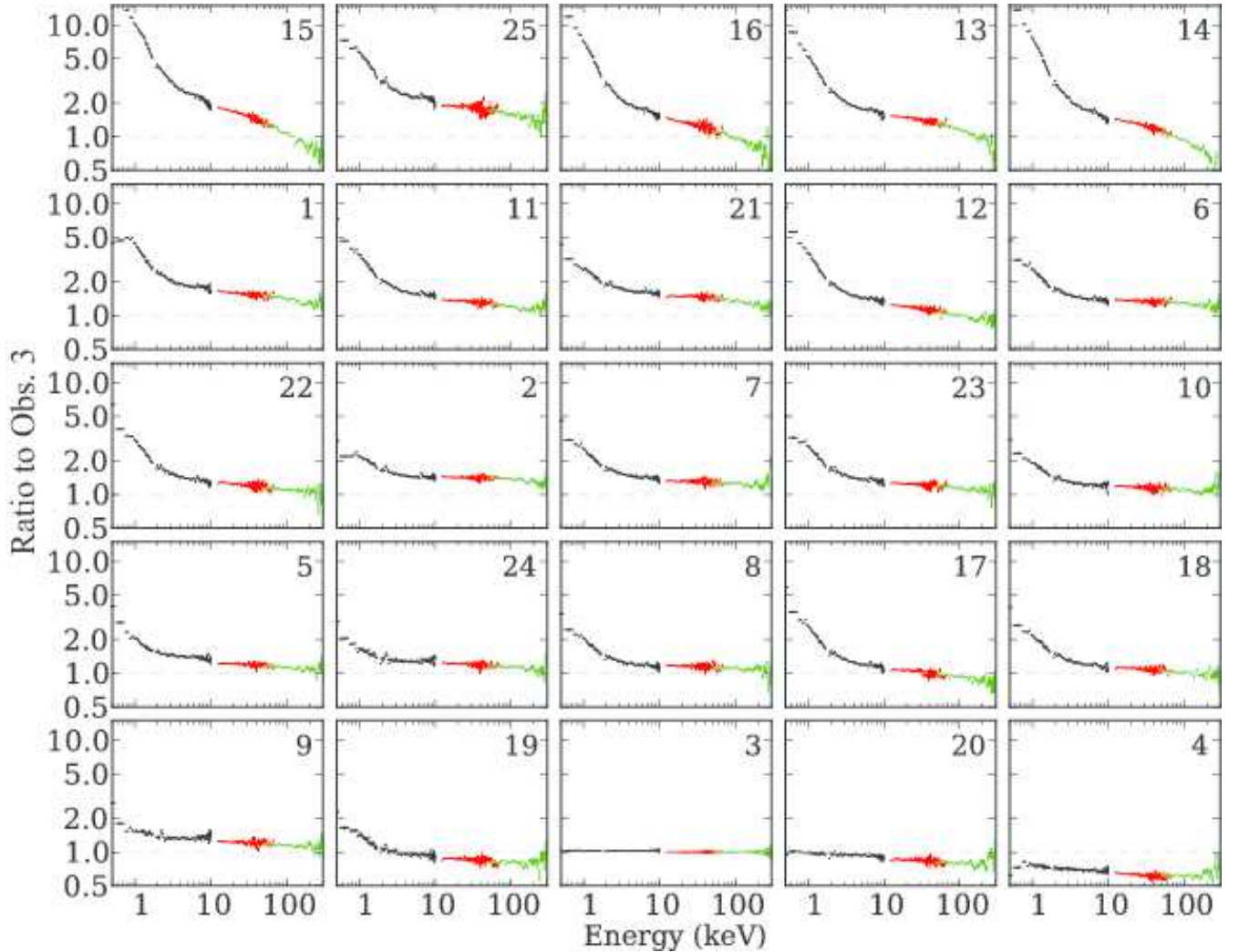


Fig. 6. The same wide-band spectra as shown in figure 5, but all normalized to that of Obs. 3.

~ 0.5 – 1 keV in all spectra. The hard intermediate state and bright low/hard state observations (top rows) show a sharp dip in variability at energies below the peak, and a moderate decrease to higher energies. By contrast, the very lowest luminosity spectral ratios (bottom row) look like the typical low/hard state but with the peak shifted to lower energies, and the variability drop to high energies appears to stop, settling to a constant variability over 3–300 keV.

4.3. Quantification of the constant disk emission

We now quantify the short-term variability suppression in $E \lesssim 2$ keV found in some observations. Assuming that the high-phase spectrum, $H(E)$, and the low-phase spectrum, $L(E)$, are decomposed into a sum of a stable soft component $d(E)$ and a varying harder component, to be denoted $h(E)$ in the former and $l(E)$ in the latter, then this can be expressed as

$$H(E) = w(E) (d(E) + h(E)) \quad (3)$$

$$L(E) = w(E) (d(E) + l(E)) \quad (4)$$

where $w(E)$ is photoelectric absorption. The spectral ratio $R(E)$ is then written as

$$R(E) \equiv \frac{H(E)}{L(E)} = \frac{d(E) + h(E)}{d(E) + l(E)}. \quad (5)$$

Since we have three unknown quantities, $d(E)$, $h(E)$, and $l(E)$, it is impossible to uniquely solve equation (5) for them. Therefore, let us assume that the ratio at $E > 2$ keV can be approximated, using two parameters α and β , as

$$R(E) \simeq \frac{h(E)}{l(E)} = \alpha E^\beta. \quad (6)$$

Supposing further that this relation between $l(E)$ and $h(E)$ can be extrapolated down to ~ 0.5 keV, equation (3) and (4) can be solved for $d(E)$ as

$$w(E)d(E) = \frac{\alpha E^\beta L(E) - H(E)}{\alpha E^\beta - 1}. \quad (7)$$

To determine α and β , we fit the spectral ratios in figure 8 with a single powerlaw over the 2–4 keV range, where the continua are not affected by the Fe-K line and edges,

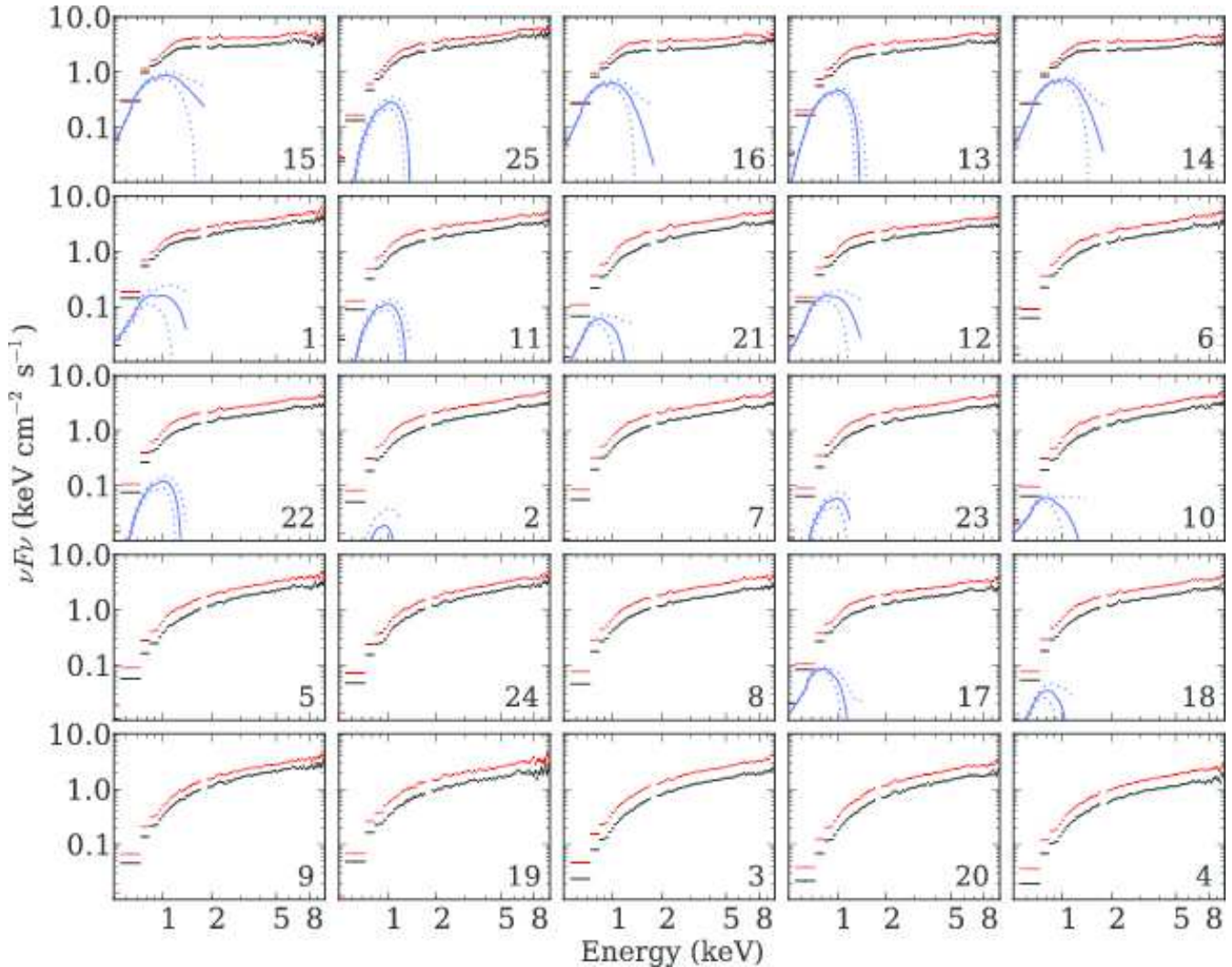


Fig. 7. The intensity-sorted νF_ν spectra of Cyg X-1, taken with XIS1. The high and low phase spectra are shown in red and black, respectively. The estimated disk component is shown in blue, with their 90% errors in dotted lines.

and summarize the best-fit parameters in table 3. Then, using equation (7) and the obtained values of α and β , we calculated $w(E)d(E)$ and show the results in figure 7 (blue). Thus, in at least 10 out of the 25 data sets (almost all the hard intermediate state and bright low/hard state and almost none of the dim low/hard state), we significantly detected a soft and stable spectral component that is responsible for the variability suppression in $\lesssim 2$ keV. The derived component exhibits a shape which is similar to that expected from low-temperature disk emission (Paper I).

To parameterize the shape of this constant component, $w(E)d(E)$, we fitted them with a `wabs * diskbb` model, with the neutral column density in $w(E)$ fixed at $7 \times 10^{21} \text{cm}^2$. The errors of $w(E)d(E)$ were defined as the two extreme values specified by allowable ranges of α and β , and are indicated in dotted lines in figure 7. The free parameters are the inner radius R_{in} and the inner disk temperature kT_{in} , which specify the total disk luminosity $L_{\text{disk}} = 4\pi R_{\text{in}}^2 T_{\text{in}}^4$, where σ is the Stefan-Boltzmann con-

stant. As summarized in table 4 and figure 9, the fit was generally successful, and yielded $kT_{\text{in}} \sim 0.1\text{--}0.2$ keV, and $R_{\text{in}} \sim 100\text{--}1000$ km, where k is the Boltzmann constant. To distinguish these from those usually obtained by fitting entire spectra, we put a subscript of “tr”, referring to a transmitted disk emission, in table 4 and figure 9.

We note that correcting the `diskbb` radii for a stress-free inner boundary condition and color temperature correction (assuming 0.41 and 1.7, respectively: Kubota et al. 2001) increases the radii only slightly by a factor of 1.18. However, the stress free inner boundary condition explicitly assumes that the disk extends down to the last stable orbit. A truncated disc may well have stress on its innermost orbit, making it more like the `diskbb` assumptions (Li et al. 2005; Gierliński, Done & Page 2008). Assuming that there is no stress correction, but that the color temperature correction stays at 1.7, then it predicts that the intrinsic radius is 2.89 ($= 1.7^2$) times bigger than that given by the `diskbb` normalization. There can also be other corrections to the inner disk ra-

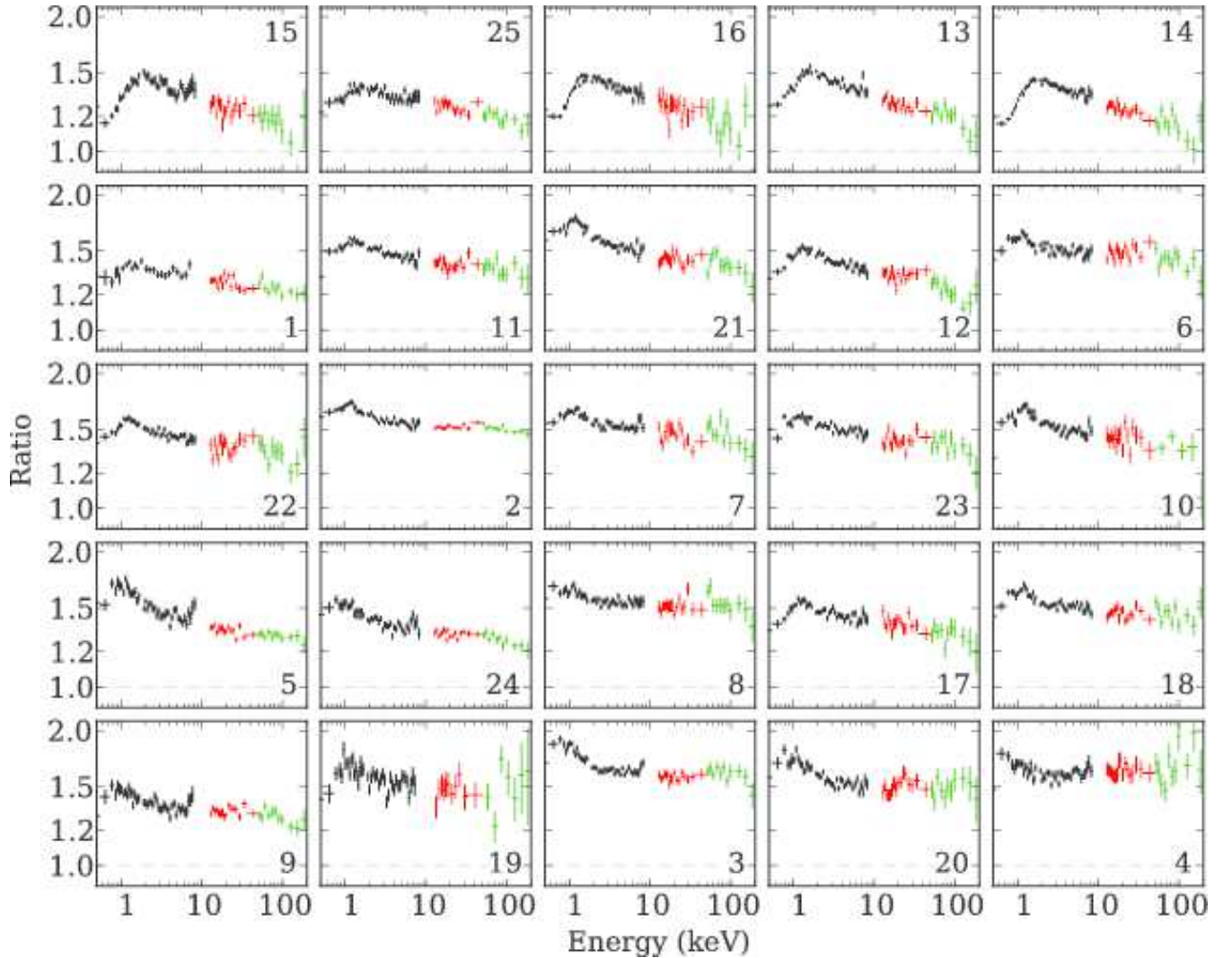


Fig. 8. The ratios between a pair of low-flux and high-flux spectra of individual observations on a time scale of 1–2 s. The colors are the same as used in figure 5.

dius, depending on how many disk photons are intercepted by the Comptonization region and its geometry with respect to the line of sight (Kubota & Done 2004; Done & Kubota 2006; Makishima et al. 2008). All these corrections act to increase the inner radius, so our estimates above using the normalization of `diskbb` are a lower limit to the size of the region contributing the constant component. For Obs. 1, we can compare the parameters of this constant component with those derived from spectral fitting of the disk in the time averaged spectrum in Paper I. The spectral fitting gives a slightly higher temperature, hence a lower radius, but just consistent given the large uncertainties. This highlights the difficulty in unambiguously separating out the disk component in these spectra. The model independent extraction used here is a more robust technique as it separates out the soft disk component from its lack of variability. These are consistent with the previous results that the disk variability is strongly suppressed above ~ 1 Hz (i.e., timescales less than 1 s) while the corona generates variability up to ~ 10 Hz (Wilkinson

& Uttley 2009; Uttley et al. 2011).

The resulting parameters of the constant disk component generally show a temperature which increases as the source brightens. The corresponding uncorrected disk inner radius is consistent with radius decreasing from 100 to $10R_g$ with increasing luminosity, but this trend is not very significant and the data could also be fairly well described by a constant radius of $\sim 20R_g$. The former case is clearly consistent with the truncated disk models, especially as all the correction factors to the radius act to substantially increase these estimated values. Even the latter case is significantly larger than the innermost stable circular orbit of a Schwarzschild black hole, so is not consistent with an untruncated disk, and especially one which is strongly illuminated in its central regions, as in the lamppost reflection models (Fabian et al. 2012). This conflicts with the much smaller radii derived from the spectral fits of Miller et al. (2012), but their adoption of a broken power law continuum gives substantially more photons in the continuum at the disk energy than a Comptonization com-

Table 3. Results of fitting the low-to-high spectral ratio in figure 8 with a single powerlaw.

N	α^*	β^*	$\chi^2(\text{d.o.f})$
1	1.429±0.027	-0.060±0.020	41.8(33)
2	1.693±0.014	-0.068±0.009	30.4(33)
3	1.749±0.018	-0.065±0.011	41.0(33)
4	1.596±0.023	-0.011±0.015	34.1(33)
5	1.650±0.024	-0.106±0.016	37.4(33)
6	1.556±0.018	-0.028±0.013	41.2(33)
7	1.622±0.016	-0.054±0.011	53.8(33)
8	1.601±0.019	-0.034±0.013	20.7(33)
9	1.445±0.024	-0.057±0.017	35.5(33)
10	1.663±0.020	-0.086±0.013	43.2(33)
11	1.596±0.016	-0.062±0.011	39.9(33)
12	1.567±0.016	-0.086±0.011	26.8(33)
13	1.582±0.015	-0.088±0.010	34.8(33)
14	1.493±0.013	-0.060±0.010	19.6(33)
15	1.484±0.020	-0.035±0.015	33.9(33)
16	1.508±0.015	-0.058±0.012	30.2(33)
17	1.543±0.017	-0.052±0.012	58.0(33)
18	1.592±0.016	-0.043±0.011	39.5(33)
19	1.735±0.041	-0.121±0.026	38.6(33)
20	1.734±0.022	-0.111±0.014	49.3(33)
21	1.736±0.018	-0.098±0.011	29.7(33)
22	1.587±0.015	-0.070±0.011	40.7(33)
23	1.615±0.016	-0.062±0.011	43.5(33)
24	1.519±0.019	-0.090±0.014	29.8(33)
25	1.426±0.018	-0.053±0.014	30.7(33)

* The values of α and β are defined as αE^β .

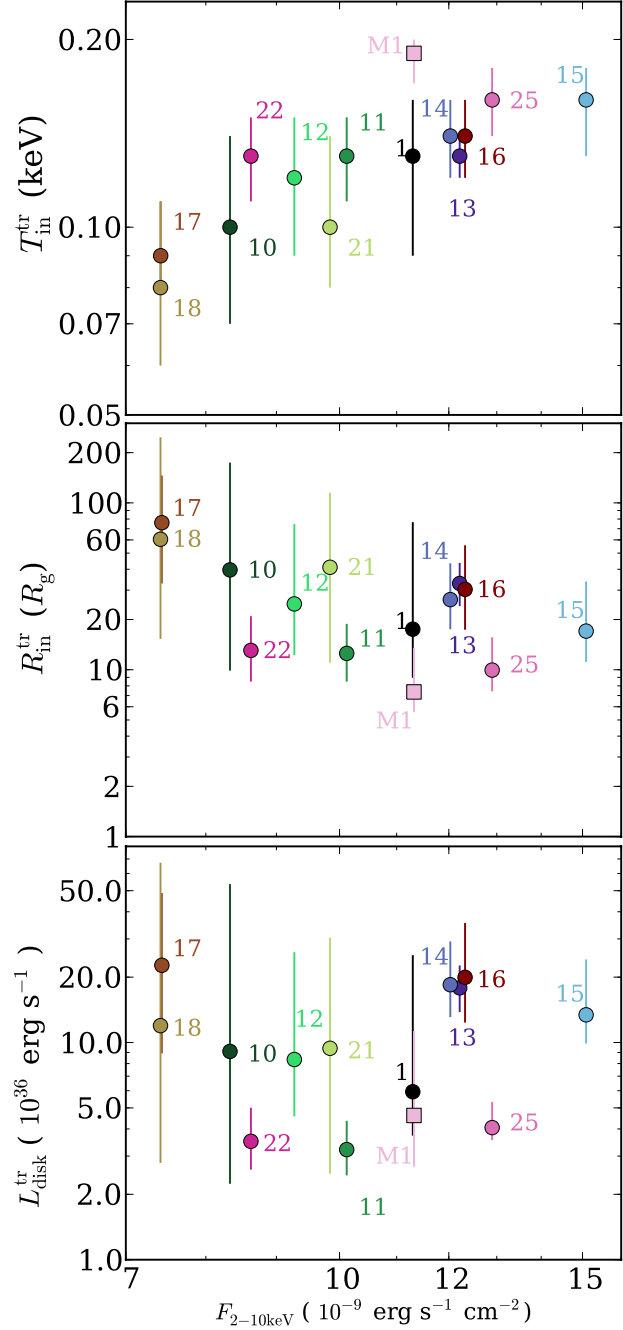
Table 4. Derived parameters of the stable disk emission.

N	$R_{\text{in}}^{\text{tr}} (R_g)$	$T_{\text{in}}^{\text{tr}} (\text{keV})$	$L^{\text{tr}*}$	$\chi^2(\text{d.o.f})$
1	17.5 ^{+59.1} _{-8.6}	0.13 ^{+0.03} _{-0.04}	5.9 ^{+19.3} _{-2.2}	0.01(11)
10	39.6 ^{+134.6} _{-29.8}	0.10 ^{+0.04} _{-0.03}	9.1 ^{+44.5} _{-6.9}	0.07(11)
11	12.5 ^{+6.3} _{-4.0}	0.13 ^{+0.02} _{-0.02}	3.2 ^{+1.1} _{-0.8}	11.48(11)
12	24.8 ^{+49.7} _{-12.6}	0.12 ^{+0.03} _{-0.03}	8.4 ^{+17.7} _{-3.8}	0.31(11)
13	32.9 ^{+10.8} _{-8.8}	0.13 ^{+0.01} _{-0.01}	17.8 ^{+4.8} _{-4.0}	17.92(15)
14	26.3 ^{+17.1} _{-8.8}	0.14 ^{+0.02} _{-0.02}	18.5 ^{+10.7} _{-5.4}	1.70(17)
15	17.0 ^{+16.8} _{-5.9}	0.16 ^{+0.02} _{-0.03}	13.4 ^{+10.7} _{-3.5}	6.34(17)
16	30.3 ^{+25.4} _{-12.9}	0.14 ^{+0.02} _{-0.02}	20.0 ^{+15.6} _{-7.6}	1.86(17)
17	76.0 ^{+69.8} _{-43.2}	0.09 ^{+0.02} _{-0.01}	22.7 ^{+26.1} _{-13.8}	4.08(10)
18	60.5 ^{+186.8} _{-45.2}	0.08 ^{+0.03} _{-0.02}	12.0 ^{+55.3} _{-9.2}	0.47(6)
21	41.1 ^{+73.7} _{-30.1}	0.10 ^{+0.04} _{-0.02}	9.4 ^{+21.0} _{-6.9}	1.12(10)
22	13.1 ^{+7.9} _{-4.6}	0.13 ^{+0.02} _{-0.02}	3.5 ^{+1.5} _{-0.9}	9.73(11)
25	9.9 ^{+5.7} _{-2.5}	0.16 ^{+0.02} _{-0.02}	4.1 ^{+1.3} _{-0.5}	9.67(11)
M1†	7.4 ^{+6.2} _{-1.8}	0.19 ^{+0.01} _{-0.02}	4.6 ^{+11.1} _{-2.0}	

* Disk luminosity in $10^{36} \text{ erg s}^{-1}$.

† Values derived by spectral fitting in Obs. 1 in Makishima et al. (2008).

ponent, suppressing their estimated disk luminosity and hence leading to a much smaller radius. Our parameters are more robustly estimated as extracting the constant component from the lightcurves means that the disk is not dependent on the assumed continuum form.

**Fig. 9.** The relation between the 0.5–10 keV flux and (a) the disk temperature, (b) the inner disk radius, and (c) the disk luminosity, listed in table 4. The result of Paper I for Obs. 1 is shown by pink squares.

4.4. Comparison of long- and short-term spectral changes

We highlight the nature of the spectral changes on long and short timescales in the hard intermediate state

(Obs 14) and relatively dim low/hard state (Obs 8) in figure 10a and b, respectively. The long timescale changes (weeks-months: blue points) are shown by the ratio of each dataset to Obs 3 (taken from figure 6), while the short timescale (seconds: red points) are the ratio of the high and low spectra from that observation (taken from figure 8).

For the hard intermediate state (Obs. 14: figure 10a) the long and short timescale ratios behave in a drastically different manner below 2 keV. The short-term variation amplitude steeply *decreases* below 2 keV, down to ~ 1.2 at ~ 0.5 keV. As already argued in section 4.3 and shown in figure 7, this can be understood as a consequence of the stable disk emission diluting low energy variability. Conversely, the long-term spectral ratio clearly *increases* towards lower energies, reaching an order of magnitude at 0.5 keV. We hence conclude that the disk emission, which lacks fast variations, evolves significantly on long time scales. Above 2 keV, the two ratios behave in a similar way (except for some differences in the amplitude). Both are characterized by spectral softening as the source gets brighter.

The dim low/hard state behavior is rather different (Obs. 8: figure 10b). Both long and short timescale ratios look very similar, being approximately constant above ~ 2 keV, then rising below this. The flatness of the short term ratio above 2 keV shows that the Comptonization component here varies predominantly in normalization only, rather than softening as it brightens.

5. Identifying a Soft Compton Emission

The previous sections have clearly identified the main characteristics of the broad band spectral evolution as an increase in disk, correlated with softening of the Compton component, and possibly a decrease in its electron temperature. Here we explore the more subtle changes indicated by the “bend” in the spectral ratios in the hard intermediate state spectra below ~ 10 keV. This could indicate an additional component beyond the disk and single temperature Comptonization continuum.

We constrain the shape of this additional emission in a model-dependent but rather robust way. We assume that the hardest component is a hard thermal Comptonization component (`compps`) and its simple reflection without fluorescence lines which is built into this code, with ionisation fixed at 0 since this cannot be constrained from the high energy data. We include also the disk component determined from the `diskbb` fits to the constant component in the previous section. We use this to fix the seed photon temperature for the Comptonization if the constant disk component is significantly detected, otherwise we fix this at 0.1 keV. We fit this model to a high energy bandpass, and then extrapolate the best-fit spectrum down to lower energies and subtract this from the data to find the excess emission over and above that expected from a single thermal Comptonization component with standard reflection.

We first choose the highest energy bandpass; i.e., we use only the data above 100 keV to determine the prop-

erties of the Comptonization region (red dotted curves in figure 11). The red dotted curve shows the model fit with (`compps`) over 100–300 keV, and the blue dotted curve is the constant disk if any, which are subtracted from the original total spectra shown in black. Figure 11 shows the resulting residual emission for Obs. 1, 3, 7 and 14 as the red spectra. The solid cyan curve superimposed on Obs. 1 in figure 11 is the shape of the additional soft Comptonization model derived by full spectral fitting in Paper I. Thus this much less model dependent approach gives results which are consistent with full spectral modeling. The residual emission (red spectra in figure 11) is rather soft with a photon index of ~ 2 –3, and increases in relative importance with increasing luminosity. The rollover at high energies is probably not significant since the residual spectrum must go to zero at 100 keV due to the assumption that the spectrum above 100 keV contains only the hard Comptonization component.

We contrast this maximal residual emission with the minimum residual emission, which is that derived from fitting the 10–300 keV PIN+GSO spectra with a single Comptonization model and its in-built reflection as in Paper II (green dotted curves in figure 11). Subtracting this, along with the constant disk component if any (blue dotted curves in figure 11), from the total spectrum (black in figure 11) results in the green spectrum shown for each observation in figure 11. This is much softer, as it must go to zero at ~ 15 keV, but still very significantly present in these spectra. Thus, if our assumption is correct, the soft Compton emission can be present between the red and green spectra in figure 11, and it is also likely that the soft Compton emission increases as the soft X-ray flux increases.

We note how the shape and the intensity of the iron line in the residual emission are quite different depending on the assumed hard component shape. Nowak et al. (2011) quantify this with four low/hard state Suzaku spectra (Obs. 1-4 here) and show that the inner radius derived from the iron line profile can significantly change with the assumed continuum form. However, here we are focussing on more robust attributes of the data, namely the continuum shape. It is clear from this analysis that there is more spectral complexity than can be modeled by a disk, single temperature Comptonization and its reflected emission. There is significantly more flux at soft energies than predicted by these models, and this additional flux increases with mass accretion rate.

Miller et al. (2012) obtained strongly reflection-dominated solutions: i.e., the ratio of reflection to power-law flux is larger than 1.0 for 10 out of 20 observations. Assuming that the reflection albedo in hard state is ~ 0.2 , this implies the reflection fraction is larger than ~ 5 (up to ~ 10 in some observations). This is inconsistent with most of previous studies that have found the reflection fraction is less than 1.0 (e.g., Gierliński et al. 1997, Paper I, and Paper II). We additionally note that it is important to separate out individual components from the spectrum in a model-independent manner, pin down their time evolution, and then reveal their origin, which may not be a

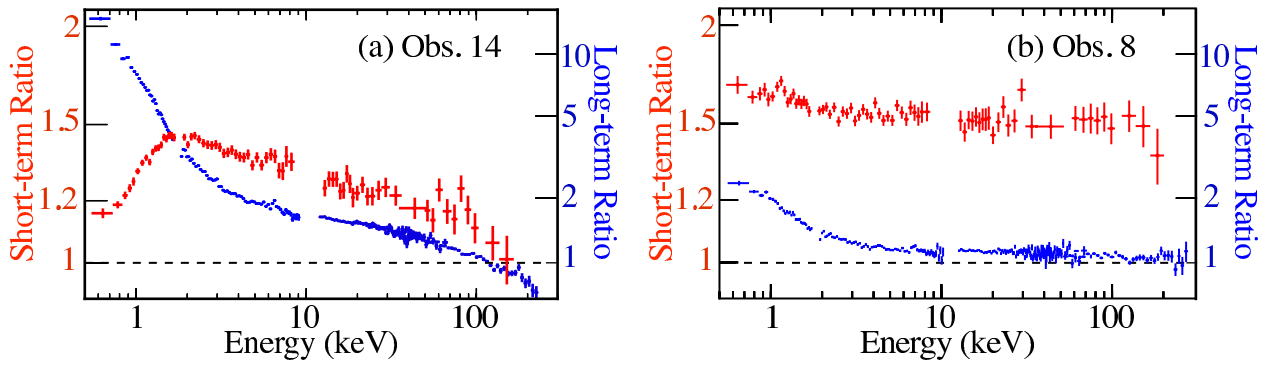


Fig. 10. A direct comparison of the long-term spectral ratio (blue) in Obs. 14 as presented in figure 6, and the short-term ratio (red), Obs. 14 vs. Obs. 3, reproduced from figure 8.

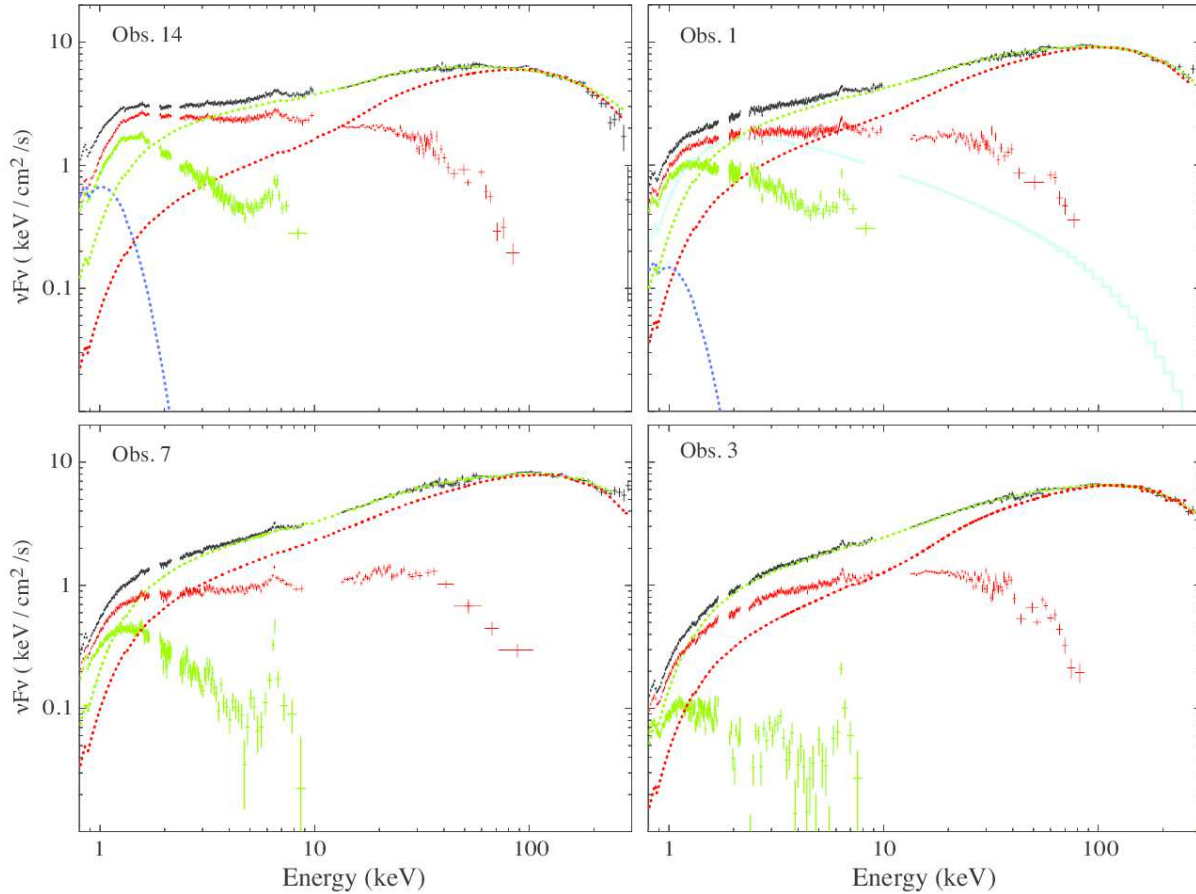


Fig. 11. The time-averaged spectra in Obs. 1, 14, 7, and 3 are shown in black (the same as figure 5). Obs. 14, 1, 7, and 3 are the descending of the soft X-ray flux. The spectra which are created by subtracting either a hard Compton component including a reflection continuum obtained by fitting over 10–300 keV (red dotted curves) or over 100–300 keV (green dotted curves), and the raw disk if any (blue dotted curves) from the time-averaged one (black) are shown in the respective color. The soft Compton spectrum used in Paper I is overlaid in cyan.

unique way but a reliable method to reach a shred of the truth.

6. Discussion

6.1. Summary of the results

We analyzed the 25 Suzaku data sets of Cyg X-1 acquired from 2005 to 2009, and successfully obtained high-quality 0.5–300 keV spectra (figure 5). The source remained in the low/hard and hard intermediate states throughout, and the unabsorbed 0.1–500 keV luminosity changed from 0.8–2.8% of the Eddington limit during the observations. Dipping periods and piled-up events were properly removed (Appendix 1 and 2).

We studied the variations of the wide-band spectra on two distinct time scales; weeks to months, and 1–2 s. The behavior shows a split between the brighter low/hard and hard intermediate state spectra, and the dimmer low/hard state spectra. We list these separately below.

The brighter low/hard and hard intermediate state:

1. The fast variability (1–2s) shows a clear separation between a constant component on a short time scale at low energies and variable tail extending to high energies. The constant low energy component is almost certainly the disk and its parameters imply that it is almost certainly truncated.
2. The spectra are more complex than can be represented by a single thermal Compton scattering component and its simple reflection. Using this model to fit the highest energy data clearly reveals additional emission with $\Gamma \sim 2\text{--}3$ which increases in importance at higher mass accretion rates.

The dimmer low/hard state:

3. The fast variability (1–2 s) does not show significant drop in $E < 2$ keV, rather peaks close to the lower limit of the XIS bandpass. The constant low energy component is thought to be rather weaker than that in the hard-intermediate state.
4. The extent of the “softer when brighter” on 1–2 s time scale is limited to $E < 3$ keV.
5. In the dimmest low/hard state (Obs. 20 and 4), they rather shows the “harder when brighter” behavior on weeks or longer time scale.

While some of these have been suggested by previous instruments, they are much more clearly shown by the Suzaku data due to its combination of broad bandpass and excellent statistics, especially as there are multiple observations tracing the behavior as a function of mass accretion rate. This is most evident in revealing the soft continuum component, which can be seen by eye in the νF_ν form (figure 5) in the hard intermediate state spectra, but which previously has been inferred only by detailed (and model dependent) spectral fitting. We discuss each of these in more detail below, and then propose a possible geometry which can explain the origin of all these components and their evolution with mass accretion rate.

6.2. Existence of the constant cool disk

We detected a sharp decrease of variability in $E \lesssim 2$ keV on a time scale of ~ 1 s in the brighter low/hard and hard intermediate states. We used this to extract the spectrum of the stable component responsible for the low-energy variability suppression, and reproduced it with a disk emission model, with a typical temperature of 0.1–0.2 keV (section 4.3). As listed in table 4, the inferred radius for this constant component is generally larger than the innermost stable circular orbit of a Schwarzschild black hole, which is not easily consistent with an untruncated disk. Conversely, it is consistent with a truncated disk, and the trend in the data (though with large uncertainties) is consistent with the truncation radius decreasing as the mass accretion rate increases as proposed by the truncated disk models.

These truncated disk models also give a framework in which to understand the lack of this stable disk component in the lowest luminosity spectra, as here the disk could be truncated at even larger radii, so its temperature is too low to significantly contribute to the spectrum above the lower limit of the XIS bandpass.

We can compare our results with theoretical expectation. In the standard disk theory (Shakura & Sunyaev 1973), the viscous time scale, t_{vis} , becomes $\gtrsim 1$ ks at $30 R_g$, assuming a typical value of $H/r \sim 0.001$ and a viscous parameter $\alpha \sim 0.1$, where H and r are the scale height and the radial distance of the disk, respectively. On the other hand, in an optically thin and geometrically thick accretion flow (Narayan & Yi 1995), we expect $t_{\text{vis}} \sim 70$ ms at $20 R_g$, assuming $\alpha \sim 0.1$ and $H/r \sim 1$. Thus, from a theoretical point of view, the disk would vary on > 1 ks, while the corona would change on a time scale of $\lesssim 1$ s. This agrees with our findings (and also Paper I) that the disk emission is more stable than the Comptonization signals.

Considering all these results, we can conclude that a cool and truncated disk is present in the XIS bandpass in the brighter low/hard state and hard intermediate state, and is stable on a time scale of ~ 1 s. Note that this constant disk is seen also in the high/soft state, where Churazov et al. (2001) showed that it can be distinguished from the variable powerlaw component on a time scale of ~ 16 s.

6.3. Long-term softening: soft Comptonization

As presented in Paper II, the spectra in $E > 10$ keV in the low/hard state can be reproduced by a hard Comptonization. Furthermore, we have obtained evidence that there is an additional soft component, and constrained its spectral shape in a model-dependent but fairly robust way (section 5: figure 11).

The origin of this component is clearly an important question. Paper I identifies this as an additional soft Comptonization component, while Nowak et al. (2011) suggests that it could be a soft component from a jet, or that the emission region is homogeneous but with an electron distribution which is more complex than a single temperature Maxwellian (see also Ibragimov et al 2005),

while Fabian et al. (2012) identify this with complex reflection in an extreme light-bending scenario. However, we can also use the fast variability information from Paper II and other studies. These clearly show that the soft leads the hard, by an amount which depends on frequency of the variability. For fixed energy bands, slow variability shows a longer hard lag than fast variability (Nowak et al. 1999; Revnivtsev et al. 1999). This can be interpreted in the context of propagating fluctuations in an inhomogeneous source, where the spectrum is harder at smaller radii (Kotov et al. 2001; Arévalo & Uttley 2006). Independent evidence for an inhomogeneous source is seen by the difference in spectral shape of the fast variability compared to the slower variability, as required in the models above (Revnivtsev et al. 1999). Thus a two Compton component model for the spectrum (e.g. Kawabata & Mineshige 2010) can also produce the observed complex variability properties. A soft jet component clearly has much more difficulty in producing the variability, as the fluctuations might be expected to propagate down through the accretion flow first, then be ejected up the jet, giving a hard lead rather than the observed lag. Similarly, soft emission from reflection should lag behind the hard illuminating component variability, though this lag time should be very short compared to the measured lags. Since a two component Comptonization model can account for both the spectrum and variability together, we favor this as the simplest model, and henceforth term the additional soft component “the soft Compton component”.

At low mass accretion rates or in the dim low/hard state, the spectral shape above ~ 3 keV remains approximately constant on a time scale of 1–2 s. The reason is that the hard Compton component dominates the spectrum above ~ 3 keV, varying mainly with its normalization; in other words, the soft Compton component in the dim low/hard state is much weaker relative to the hard Compton component. Conversely, it is the increasing dominance of the soft Compton component in the hard intermediate state which leads to the abrupt softening on the color-intensity diagram which is the defining characteristic of this state (figure 2b). These features suggest that the soft Comptonization component probably has different time variability, characterized by “softer when brighter”.

Therefore, the present results significantly strengthen the idea of multi-zone Comptonization presented in Paper I. A new implication obtained here is that the soft Comptonization changes more than the hard Comptonization on the long time scale, possibly following more faithfully the accretion-rate changes.

6.4. Where do soft seed photons come from?

In the hard intermediate state, the spectra become softer and show decrease of fast variability in $E < 2$ keV as shown in figure 8 when it gets brighter. This trend is the same as found in Paper I, and thus the interpretation proposed in Paper I that the seed photons are put into the inhomogeneous corona above the disk can be valid. On the other hand, the break energy in the spectral ra-

tios on a time scale of ~ 1 s in figure 8, decreases from ~ 2 keV in the hard intermediate state to < 0.5 keV in the dim low/hard state, as the soft X-ray flux decreases. The new observational fact requires supplemental explanation to the physical interpretation proposed in Paper I. This might appear to be simply explained by the increase of the truncation radius and the decrease of the disk temperature. However, the soft excess in $E < 2$ keV can be clearly recognized in figure 12 by looking into the time-averaged νF_ν spectra after removing the typical interstellar absorption of $N_H = 7 \times 10^{21}$ cm². Furthermore, the variability in $E < 2$ keV does not decrease, but rather increases (Obs. 3, 20, and 4 in figure 8). Therefore, the spectrum should include some extent of variable soft emission, which can not be separated out on 1–2 s time scale as a constant disk component. This is consistent with a soft component inferred from detailed spectral fits to the low/hard state data; e.g., according to Nowak et. al (2011), the spectra in Obs. 2 and 3 show a clear need for a thermal component at low energies, yet this is not seen as a constant component in our analysis.

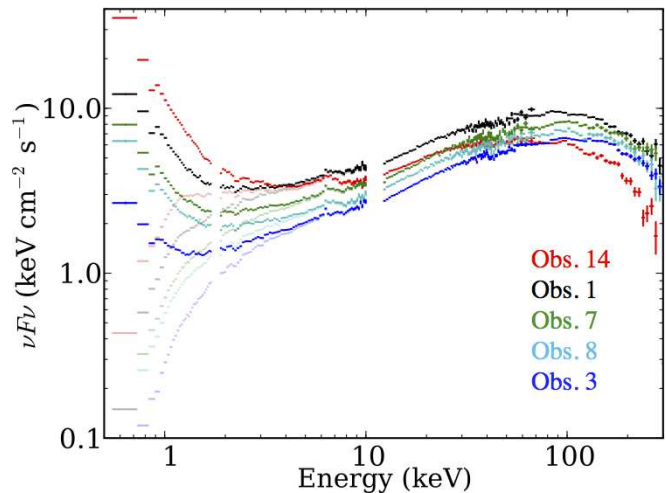


Fig. 12. Several representative νF_ν spectra after removing interstellar absorption. In comparison, those before removing interstellar absorption are shown in faint colors.

The variable soft component, if its spectral shape is similar to disk emission, would probably have a slightly higher temperature than the (unseen) constant disk component, because the disk temperature should be higher than ~ 0.1 keV to create soft excess up to ~ 1 keV. The simplest interpretation within a framework of the “disk-corona” configuration would be that the disk interacts more strongly with the corona in the dim low/hard state than in the hard-intermediate state, leaving less stable disk-like component in the dim low/hard state, but providing some amount of seed photons for the corona in a time-varying way, presumably at an overlapping region between the disk and the corona. The slight “softer when brighter” behavior around 0.5–2 keV in the dim low/hard state might be some hint of variable soft emission if it is indeed produced by Comptonization (Gierliński & Zdziarski 2004).

Alternatively, the source of seed photons might be different when accretion rate is low, e.g., synchrotron emission (Wardziński & Zdziarski 2000; Veledina et al. 2011a,b). In addition to the different short-term behavior in $E < 2$ keV, the faintest Obs. 3, 20, and 4 with $L \sim 1\% L_{\text{Edd}}$ exhibit somewhat anomalous long-term spectral changes over the entire 0.5-200 keV range; the spectrum *softens* as the source gets dimmer (figure 6). This behavior is commonly seen in other black hole binaries at $L \lesssim 1\% L_{\text{Edd}}$ (Yamaoka et al. 2005; Yuan et al. 2007; Wu & Gu 2008; Russell et al. 2010; Sobolewska et al. 2011; Armas Padilla et al. 2013). The ratio fluxes during our observations taken in 2009 are monitored with the Arcminute MicroKelvin Array radio telescope (Zwart et al. 2008). The 12–70 keV X-ray and ratio fluxes are positively correlated, as shown in figure 4 in Miller et al. (2012). Thus, it does not indicate the increase of synchrotron radiation, but imply the possibility that seed photons start to be more provided by cyclo-synchrotron radiation than the truncated stable disk when $L \lesssim 1\% L_{\text{Edd}}$ (Sobolewska et al. 2011; Gardner & Done 2012).

6.5. Disk and Inhomogeneous Coronae configuration

We can put all these together if the spectrum contains a constant disk, a variable soft Compton component which softens as it brightens on short timescales, and a variable hard Compton component which changes mostly in normalization, and possibly the additional variable disk-like component. As found in the dim low/hard state, the disk is truncated far from the black hole, so its temperature is below the lower end of the XIS bandpass. Increasing the mass accretion rate gives an increasing temperature and luminosity from the constant disk, increasing its impact on the XIS spectrum. This produces the characteristic drop in fast variability at low energies seen increasingly at higher luminosities.

The fraction of the flow in the soft Comptonization regime, which is presumably generated from overlapping region between the disk and corona, increases with mass accretion rate. The soft Compton comes to dominate the spectrum below 10 keV in the hard intermediate state, but only makes a much smaller contribution, extending only to ~ 2 keV in the dim low/hard state. Fast variability supports this, because the spectrum is “softer when brighter” in the hard intermediate state while almost no change in shape in the dimmer low/hard state.

We sketch this changing geometry in figure 13. We propose that this is a universal geometry for the low/hard and hard intermediate states as wide-band Suzaku spectra of GRO J1655-40 (Takahashi et al. 2008) and GX 339-4 (Shidatsu et al. 2011) were also well reproduced with the double-Compton modeling, which includes a disk with $kT_{\text{in}} \sim 0.2$ keV.

As mentioned in section 6.4, the constant truncated disk is likely to be accompanied by a variable soft component, which might be originated from highly unstable disk-corona interaction or a variable cyclo-synchrotron radiation or else. It would be possible to speculate perhaps clumps torn off the disk edge (Chiang et al. 2010). These

clumps would be variable, as they are continually removed by being accreted and/or dissipated/evaporated, but are also continually replenished by new clumps forming. They are likely to have a higher temperature, and smaller emitting area than the constant disk component. Thus they are still visible in the spectrum when the constant disk has too low a temperature to contribute to the observed bandpass, as in the dim low/hard state. These would also be closer (embedded into?) the Comptonising region, so that they can efficiently put seed photons for the Comptonization.

6.6. Analogies to massive black holes

The primary emission from active galactic nuclei, AGNs, which is also regarded as Comptonization based on the analogy of the black hole binaries, should be understood before decoding reprocessed or secondary emission in detail. Recently, Suzaku spectra of the typical Seyfert galaxy Mrk 509 have been reproduced by two-component Comptonization (Noda et al. 2011b; Mehdipour et al. 2011). Noda et al. (2011a) analyzed Suzaku data of MCG-6-30-15, and found a secondary component that is different in variation properties from the dominant powerlaw. Similar components are reported in different types of AGNs (Noda et al. 2013). A more likely contender for similar behavior is the typical low-luminosity AGN; e.g., “softer when brighter” behavior is seen in NGC 4258 (Yamada et al 2009), while “harder when brighter” in NGC 7213 (Emmanoulopoulos et al. 2012). Although these samples are not enough, future missions, which have wider spectral coverage with higher sensitivity, such as ASTRO-H (Takahashi et al. 2010), enable us to reveal the nature of the disk-coronae picture around a massive black hole.

7. Conclusion

We investigate the spectral evolution via model-independent analysis of the long and short timescale variability. Our results are summarized as follows:

- A cool disk component exists almost certainly in the low/hard state, which increases in luminosity and temperature as the luminosity increases. The disk parameters imply that it is truncated, and are consistent with radius decreasing as the luminosity increases.
- The bright low/hard state spectra show a clear break at ~ 10 keV on long time scales, as opposed to the lower luminosity spectra, where the 3-300 keV tail is consistent with a single Compton component (and its simple reflection). This can be interpreted as two separate Compton components, one hard and the other soft Compton component as obtained in Paper I.
- On long timescales, the soft Compton component increases along with the cool disk component, while the hard Compton does not change by much at all. Thus the hard intermediate spectra are dominated by the soft Compton component at least up

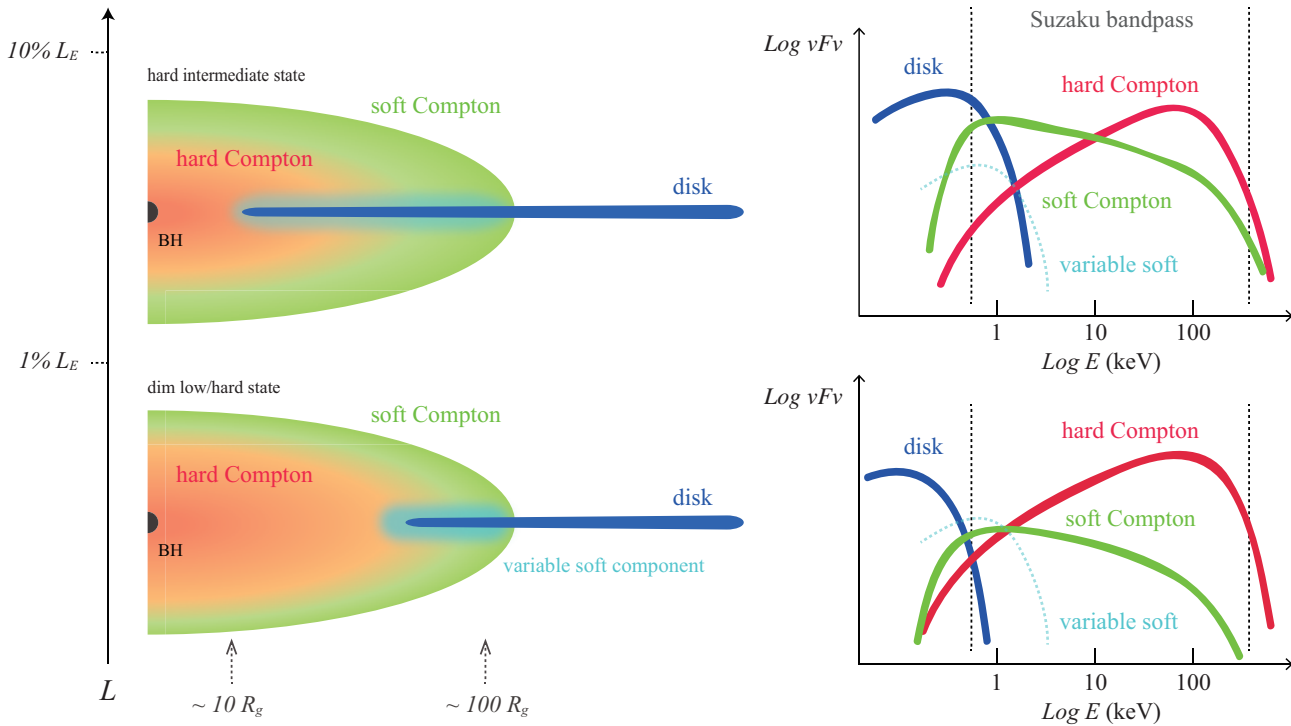


Fig. 13. Conceivable accretion flows (left) and spectral composition in νF_ν form (right) in the hard intermediate state (top) and the dim low/hard state (bottom). Some gross representative values on luminosities and radii are overlaid on the flow pictures. The disk, hard Compton, soft Compton, and variable soft component are indicated by blue, red, green, and cyan, respectively. Fe-K lines and reflection components, which presumably come from the disk, are not depicted just for simplicity.

to $\sim 3\text{--}30$ keV, with the hard Compton component dominating at the highest energies, while the dim low/hard state is dominated by the hard Compton component from 3–300 keV.

- An additional, variable, source of seed photons is implied in the dim low/hard state based on the lack of decrease in variability as shown in figure 8 and the variable soft excess as shown in figure 12. Conceivable accretion flows are presented in figure 13.

Thus there can be potentially four components in the Suzaku bandpass: a cool truncated disk which is constant, a variable soft blackbody-like component, a soft Compton component from the outer flow and a hard Compton component from the inner flow. Spectral fitting alone is unlikely to uniquely separate out all these component and we urge a combined spectral-timing approach in order to robustly interpret such complex data.

Acknowledgement

The authors would like to express their thanks to Suzaku team members. The research presented in this paper has been financed by Grant-in-Aid for JSPS Fellows. S.Y. is supported by the Special Postdoctoral Researchers Program in RIKEN. This work was supported by JSPS KAKENHI Grant Number 24740129.

Appendix 1. Orbital phase and exclusion of dipping periods

In table 1, we summarize the orbital phases of all Suzaku observations. Since photo absorption caused by dips significantly affects soft X-rays, we need to properly exclude the dip phases. We have folded the hardness ratios (table 1) of ASM according to the orbital period, where data points were discarded while the object is in the high/soft state. The orbital period $P = 5.599829$ days and an epoch of the superior conjunction of the black hole at MJD41874.207 are used, based on Brocksopp et al. (1999). Figure 14 shows the results of this analysis. At the near phase 0 (i.e., when the observer, the companion star, and Cyg X-1 are in line with this order), the hardness ratio increases by $\sim 20\%$ due to increased absorption. This modulation has been studied by many authors (e.g., Poutanen et al. 2008).

We overlaid the hardness ratios at the 25 observations in figure 14. Our observations are thus evenly distributed over the orbital phase. The scatter of the hardness ratio is much larger than that caused by the orbital modulation, so that the effect seen among the Suzaku observations can be considered as a result of intrinsic spectral changes of Cyg X-1.

As seen in figure 14, some of the observations are observed around phase 0., which are likely suffered from sig-

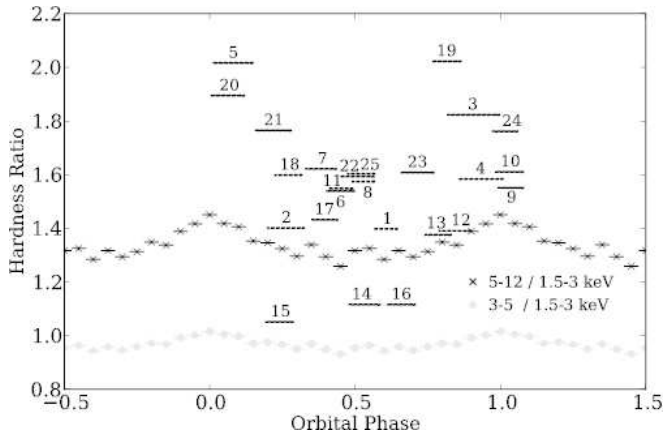


Fig. 14. The hardness ratio of ASM of Cyg X-1 folded by the orbital period of 5.6 days. Two phases are shown for clarity. Phase 0 is defined as the superior conjunction, when the black hole is the farthest from us. The corresponding Suzaku observations are indicated, with their vertical positions representing the 5–12/1.5–3 keV hardness ratio. The phase coverage by each Suzaku observation is indicated by the length of each segment.

nificant dips. Thus, we need to exclude the dipping period during observation. We constructed three-band (0.5–1.5, 1.5–3.0, and 3.0–10.0 keV) light curves for the same XIS used in figure 3. These light curves were utilized for studying the source motion on a “softness-softness plot” in figure 15, in which the ratio of 1.5–3.0 keV to 3.0–10.0 keV count rate plotted against that of 0.5–1.5 keV to 1.5–3.0 keV count rate. The dips start with an increase of the neutral absorption, followed by an enhanced contribution by an ionized or partial-covering absorber. The former effect brings the data points toward lower left, while the latter toward lower right due to recovery of the softest counts. These dips last for several hours, causing significant drops in the soft X-ray flux. It has already been reported that neutral column density changed from $\sim 5 \times 10^{21} \text{ cm}^{-2}$ to $\sim 5 \times 10^{22} \text{ cm}^{-2}$ in Obs. 3, 4, and 5 (Nowak et al. 2011).

We define “dipping periods”, as those time bins wherein the data on the softness plot is outside a circle with a radius of 0.2, centered on the distribution centroid. These periods are indicated in light gray in figure 15. Throughout the paper, we used the period excluding the dipping phase.

Appendix 2. Attitude correction and pileup estimation of the XIS data

Due to thermal wobbling of the XRT, the center of the images fluctuates by $\sim 1'$, depending on day or night for the satellite, on a time scale of ~ 45 minutes (half the orbital period of the satellite). Since this affects significantly the fraction of the photons (Uchiyama et al. 2008), the 1/4 window option has been used since Obs. 3. A correction software, `aattcor` (Uchiyama et al. 2008), has been developed to correct the attitude solution for the thermal wobbling. However, even after processed with this software, there still remains attitude fluctuation by

$\sim 30''$. We further corrected the image for the residual fluctuation, and reduced them to be ~ 5 pixel ($\sim 5''$). More details on the attitude correction are summarized in Yamada et al. (2012).

In general, the extent of the pileup effect is proportional to the incoming flux squared, because the phenomenon is a kind of process of two-particle collision. The process is irreversible, and thus there is no straightforward ways to estimate the pileup effects. We have utilized several phenomenological approaches for bright point sources to estimate the pileup effects; e.g., surface brightness, hardness, and grade branching ratio.

Based on the analyses, we compiled a pileup estimation software, `aepileupcheckup.py` which returns the radii at which pileup fraction (cf. eq (1) in Yamada et al. 2012) becomes 3% and 1%. Table 5 summarizes the exposure excluding the telemetry-saturated period, the two radii corresponding to $R_{3\%}$ and $R_{1\%}$, the 0.5–10.0 keV count rates for a circle within a radius of $4'$, outside $R_{3\%}$ and $R_{1\%}$. The differences in exposure among the XIS cameras are due to differences of their allocated telemetry quota and the employed editing modes.

Appendix 3. Count rates of the HXD data

Table 6 gives the exposures of the HXD data corrected for dead time, and NXB-subtracted count rates in four energy bands. The dead time fraction was estimated by using “pseudo” events (Kokubun et al. 2007). The observed count rates in Obs. 1 are apparently higher by $\sim 10\%$ than the others, because the effective area is higher by $\sim 10\%$ in the HXD nominal position employed in that observation than in the XIS nominal position.

The lower threshold of PIN was gradually raised to avoid enhanced noise since Obs. 6, which reduces the effective area of the PIN over 10–15 keV. Thus, the count rates in $E > 15$ keV are shown in table 6.

References

- Arévalo, P., & Uttley, P. 2006, MNRAS, 367, 801
- Armas Padilla, M., Degenaar, N., Russell, D. M., & Wijnands, R. 2013, MNRAS, 428, 3083
- Beloborodov, A. M., 1999, ApJ, 510L, 123
- Brocksopp, C., Fender, R. P., Larionov, V., et al. 1999, MNRAS, 309, 1063
- Caballero-Nieves, S. M., 2009, ApJ, 701, 1895
- Chiang, C. Y., Done, C., Still, M., & Godet, O. 2010, MNRAS, 403, 1102
- Churazov, E., Gilfanov, M., & Revnivtsev, M. 2001, MNRAS, 321, 759
- Dotani, T., et al. 1997, ApJ, 485, L87
- Di Salvo, T., Done, C., Zycki, P. T., Burderi, L., & Robba, N. R. 2001, ApJ, 547, 1024
- Done, C., & Kubota, A. 2006, MNRAS, 371, 1216
- Done, C., Gierliński, M., & Kubota, A. 2007, A&A Rev., 15, 1
- Emmanoulopoulos, D., Papadakis, I. E., McHardy, I. M., et al. 2012, MNRAS, 424, 1327
- Fabian, A. C. et al., 2012, MNRAS, 424, 217

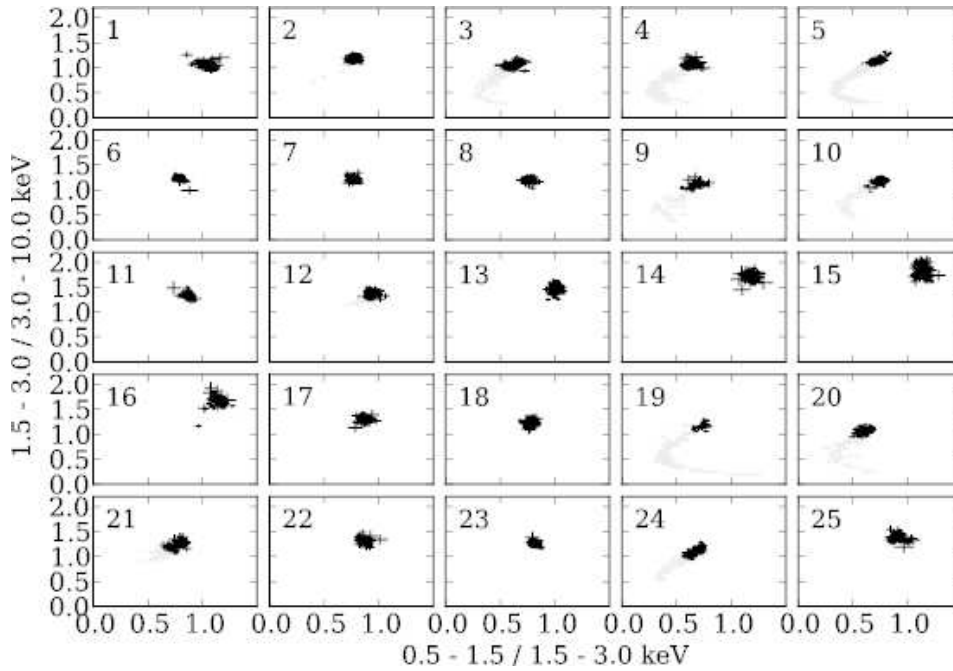


Fig. 15. The 0.5–1.5 to 1.5–3.0 keV softness vs. the 1.5–3.0 to 3.0–10.0 keV softness plot, for 128 s binning. The grey data points define the dipping period, while the black ones represent normal periods.

- Fender, R. P., Belloni, T. M., & Gallo, E. 2004, MNRAS, 355, 1105
- Fender, R. P., Stirling, A. M., Spencer, R. E., et al. 2006, MNRAS, 369, 603
- Frontera, F., et al. 2001, ApJ, 546, 1027
- Fukazawa, Y., et al. 2009, PASJ, 61, 17
- Gardner, E., & Done, C. 2012, MNRAS, *inpress*
- Gierliński, M., Zdziarski, A. A., Done, C., et al. 1997, MNRAS, 288, 958
- Gierliński, M., Zdziarski, A. A., Poutanen, J., et al. 1999, MNRAS, 309, 496
- Gierliński, M., & Zdziarski, A. A. 2005, MNRAS, 363, 1349
- Gierliński, M., Done, C., & Page, K. 2008, MNRAS, 388, 753
- Gilfanov, M., Churazov, E., & Revnivtsev, M. 1999, A&A, 352, 182
- Gilfanov, M., Churazov, E., & Revnivtsev, M. 2000, MNRAS, 316, 923
- Gou, L, et al., 2011, ApJ, 742, 85
- Haardt, F., Maraschi, L., 1991, ApJ, 380, L51-L54
- Homan, J., & Belloni, T. 2005, Ap&SS, 300, 107
- Ibragimov, A., Poutanen, J., Gilfanov, M., Zdziarski, A. A., & Shrader, C. R. 2005, MNRAS, 362, 1435
- Ichimaru, S. 1977, ApJ, 214, 840
- Ishisaki, Y., et al., 2007, PASJ, 59, 113
- Kawabata, R., & Mineshige, S. 2010, PASJ, 62, 621
- Kubota, A., & Done, C. 2004, MNRAS, 353, 980
- Kokubun, M., et al. 2007, PASJ, 59, 53
- Koyama, K., et al. 2007, PASJ, 59, 23
- Kubota, A., Done, C., Davis, S. W., et al. 2010, ApJ, 714, 860
- Kitamoto, S., Miyamoto, S., Tanaka, Y., et al. 1984, PASJ, 36, 731
- Kotov, O., Churazov, E., & Gilfanov, M. 2001, MNRAS, 327, 799
- Liang, E. P. T., & Price, R. H. 1977, ApJ, 218, 247
- Li, L.-X., Zimmerman, E. R., Narayan, R., & McClintock, J. E. 2005, ApJS, 157, 335
- Magdziarz, P., Blaes, M. O., Zdziarski, A. A., Johnson, W. N., & Smith, D. A., 1998, MNRAS, 301, 179
- Makishima, K., Maejima, Y., Mitsuda, K., et al. 1986, ApJ, 308, 635
- Makishima, K., et al. 2008, PASJ, 60, 585
- Miller, J. M., Pooley, G. G., Fabian, A. C., et al. 2012, ApJ, 757, 11
- Mitsuda, K., et al. 1984, PASJ, 36, 741
- Mitsuda, K., et al. 2007, PASJ, 59, 1
- Miyamoto, S., & Kitamoto, S. 1989, Nature, 342, 773
- Miyamoto, S., Kitamoto, S., Iga, S., Negoro, H., & Terada, K. 1992, ApJL, 391, L21
- Mehdipour, M., et al. 2011, A&A, 534, A39
- Narayan, R., & Yi, I. 1995, ApJ, 444, 231
- Negoro, H., Kitamoto, S., Takeuchi, M., and Mineshige, S., 1995, 452, L49
- Noda, H., et al. 2011a, PASJ, 63, 449
- Noda, H., et al. 2011b, PASJ, 63, 925
- Noda, H., et al. 2013, PASJ, 65, 4
- Nowak, M. A., Vaughan, B. A., Wilms, J., Dove, J. B., & Begelman, M. C. 1999, ApJ, 510, 874
- Nowak, M. A., et al. 2011, ApJ, 728, 13
- Oda, M., Gorenstein, P., Gursky, H., et al. 1971, ApJL, 166, L1
- Orosz, J. A., & Hauschildt, P. H. 2000, A&A, 364, 265
- Orosz, J. A., McClintock, J. E., Aufdenberg, J. P., et al. 2011, ApJ, 742, 84
- Poutanen, J., Vilhu, O., 1993, A&A, 275, 337
- Poutanen, J., & Svensson, R. 1996, ApJ, 470, 249
- Poutanen, J., Zdziarski, A. A., & Ibragimov, A. 2008, MNRAS, 389, 1427
- Revnivtsev, M., Gilfanov, M., & Churazov, E. 1999, A&A, 347, L23
- Reid, M. J., McClintock, J. E., Narayan, R., et al. 2011, ApJ, 742, 83
- Remillard, R. A., & McClintock, J. E. 2006, ARA&A, 44, 49

Table 5. The exposures, estimated $R_{3\%}$ and $R_{1\%}$, and corresponding count rates for each XIS.

N	XIS0			XIS1			XIS3		
	E^* (ks)	$R_{3,1\%}^\dagger$	$C_{a,3,1\%}^\ddagger$	E (ks)	$R_{3,1\%}$	$C_{a,3,1\%}$	E (ks)	$R_{3,1\%}$	$C_{a,3,1\%}$
1 [§]	10.5	74, 109	280, 67, 18	3.5	56, 127	241, 124, 20	6.9	70, 135	298, 101, 23
2	8.3	21, 50	216, 163, 77	8.2	17, 50	233, 206, 116	8.3	23, 51	246, 182, 93
3	11.3	18, 49	145, 122, 74	11.3	11, 48	156, 149, 102	11.3	21, 53	168, 139, 86
4	8.3	8, 35	95, 89, 61	8.3	6, 32	102, 100, 78	8.3	10, 38	109, 102, 70
5	-	-	-	8.5	19, 56	197, 175, 112	8.5	25, 61	205, 160, 91
6	3.8	31, 71	264, 186, 88	3.8	30, 79	299, 240, 116	3.8	36, 75	303, 203, 99
7	5.3	30, 70	250, 180, 86	5.3	27, 78	273, 227, 108	5.3	34, 74	285, 201, 98
8	4.3	27, 62	212, 160, 87	4.3	24, 72	240, 205, 107	4.3	30, 68	242, 178, 93
9	-	-	-	4.5	18, 57	203, 185, 119	-	-	-
10	5.1	27, 61	214, 160, 87	5.1	22, 69	233, 205, 112	5.1	31, 68	252, 184, 97
11	4.9	35, 74	300, 203, 95	4.8	36, 89	352, 270, 119	4.9	39, 82	353, 235, 109
12	5.3	34, 72	282, 192, 94	5.3	36, 87	336, 256, 114	5.3	38, 78	333, 222, 109
13	5.2	44, 84	385, 230, 99	5.1	46, 101	448, 311, 109	5.0	50, 90	447, 254, 115
14	6.9	50, 90	429, 235, 99	6.1	51, 105	496, 331, 117	5.5	56, 94	479, 251, 116
15	3.6	61, 99	522, 242, 100	2.8	62, 111	597, 342, 127	2.7	62, 103	565, 269, 115
16	4.2	46, 88	418, 242, 99	4.1	49, 101	484, 327, 128	4.0	55, 92	479, 251, 118
17	5.1	29, 65	226, 167, 89	5.1	27, 75	261, 215, 108	5.1	32, 71	258, 183, 93
18	5.8	29, 64	221, 163, 88	5.8	27, 74	256, 211, 108	5.8	31, 69	248, 179, 92
19	5.3	10, 40	112, 105, 68	5.6	7, 40	129, 125, 90	5.7	14, 44	131, 117, 76
20	6.5	16, 47	135, 119, 75	6.5	10, 44	143, 137, 95	6.5	18, 50	150, 128, 78
21	5.8	34, 72	280, 193, 95	5.9	34, 85	317, 243, 109	6.0	37, 76	324, 214, 103
22	5.4	33, 71	272, 189, 95	5.6	34, 84	315, 240, 109	5.6	37, 74	309, 205, 101
23	5.5	33, 67	260, 182, 97	5.6	32, 84	297, 232, 104	5.6	36, 72	294, 198, 102
24	4.7	26, 62	192, 153, 83	5.4	24, 65	225, 194, 112	-	-	-
25	2.7	48, 90	407, 232, 95	5.4	51, 96	457, 281, 114	-	-	-

* The exposure after removing the periods of telemetry saturation.

† In units of pixel, where 1 pixel is 1.042".

‡ The count rates integrated over a circle with a radius of 4', and outside $R_{3\%}$ and $R_{1\%}$.

§ $R_{3\%}$ and $R_{1\%}$ of XIS2 are 87, 125 pixel, 11.2 ks, 292.0, 56.6, 18.2 counts s⁻¹.

|| $R_{3\%}$ and $R_{1\%}$ of XIS2 are 23, 53 pixel, 8.3 ks, 257.1, 196.0, and 97.4 counts s⁻¹.

- Ross, R. R., & Fabian, A. C. 2005, MNRAS, 358, 211
 Serlemitsos, P. J., et al. 2007, PASJ, 59, 9
 Shakura, N. I., & Sunyaev, R. A. 1973, A&A, 24, 337
 Shapiro, S. L., Lightman, A. P., & Eardley, D. M. 1976, ApJ, 204, 187
 Shidatsu, M., et al. 2011, PASJ, 63, 785
 Sobolewska, M. A., Papadakis, I. E., Done, C., & Malzac, J. 2011, MNRAS, 417, 280
 Sunyaev, R. A., & Trümper, J. 1979, Nature, 279, 506
 Takahashi, K., Inoue, H., & Dotani, T. 2001, PASJ, 53, 1171
 Takahashi, H., et al. 2008, PASJ, 60, 69
 Takahashi, T., et al. 2007, PASJ, 59, 35
 Takahashi, T., et al. 2010, Proc. SPIE, 7732,
 Tananbaum, H., Gursky, H., Kellogg, E., Giacconi, R., & Jones, C. 1972, ApJL, 177, L5
 Thorne, K. S., & Price, R. H. 1975, ApJL, 195, L101
 Torii, S., Yamada, S., Makishima, K., et al. 2011, PASJ, 63, 771
 Uchiyama, Y., et al. 2008, PASJ, 60, 35
 Uttley, P., Wilkinson, T., Cassatella, P., et al. 2011, MNRAS, 414, L60
 Veledina, A., Vurm, I., & Poutanen, J. 2011a, MNRAS, 414, 3330
 Veledina, A., Poutanen, J., & Vurm, I. 2011b, ApJL, 737, L17
 Wang, J.-M., Cheng, C., & Li, Y.-R. 2012, ApJ, 748, 147
 Wilkinson, T., & Uttley, P. 2009, MNRAS, 397, 666
 Xiang, J., Lee, J. C., Nowak, M. A., & Wilms, J. 2011, ApJ, 738, 78
 Yamada, S. et al., 2009, ApJ, 707L, 109
 Yamada, S. 2011, Ph.D. Thesis,
 Yamada, S., et al. 2011, PASJ, 63, 645
 Yamada, S., et al. 2012, PASJ, 64, 53
 Yamaoka, K., Uzawa, M., Arai, M., Yamazaki, T., & Yoshida, A. 2005, Chinese Journal of Astronomy and Astrophysics Supplement, 5, 273
 Yuan, F., Zdziarski, A. A., Xue, Y., Wu, X., 2007, ApJ, 659, 541
 Wardziński, G., Zdziarski, A. A., 2000, MNRAS, 314, 183
 Zdziarski, A. A., Poutanen, J., Mikolajewska, J., et al. 1998, MNRAS, 301, 435
 Zdziarski, A. A., Poutanen, J., Paciesas, W. S., & Wen, L. 2002, ApJ, 578, 357
 Zdziarski, A. A., & Gierliński, M. 2004, Progress of Theoretical Physics Supplement, 155, 99
 Zwart, J. T. L., Barker, R. W., Biddulph, P., et al. 2008, MNRAS, 391, 1545

Table 6. The exposures and count rates of Cyg X-1 recorded with the HXD.

N	Exposure Time(ks)*	PIN		GSO		F_{10-200}^{\ddagger}
		$C(15-20 \text{ keV})^{\dagger}$	$C(20-60 \text{ keV})^{\dagger}$	$C(50-100 \text{ keV})^{\dagger}$	$C(100-200 \text{ keV})^{\dagger}$	
1	16.8 (92.9)	12.61±0.03 (1.0)	15.06±0.03 (1.2)	17.30±0.04 (19.0)	8.94±0.03 (36.2)	4.14
2	25.8 (93.1)	11.91±0.02 (1.1)	14.24±0.02 (1.4)	17.67±0.03 (26.4)	9.63±0.03 (46.5)	3.88
3	37.4 (93.0)	8.39±0.02 (1.4)	10.07±0.02 (1.9)	12.61±0.03 (34.4)	7.17±0.03 (56.2)	2.80
4	30.4 (93.4)	5.33±0.01 (2.2)	6.27±0.01 (3.0)	7.75±0.03 (45.2)	4.39±0.03 (67.0)	1.73
5	27.0 (93.3)	10.06±0.02 (1.1)	12.05±0.02 (1.6)	14.49±0.03 (32.2)	7.88±0.03 (56.0)	3.24
6	14.4 (92.7)	11.32±0.03 (0.9)	13.58±0.03 (1.2)	16.62±0.05 (30.5)	9.06±0.05 (54.1)	3.70
7	12.2 (92.9)	10.82±0.03 (1.1)	13.13±0.03 (1.4)	15.89±0.05 (31.9)	8.81±0.05 (55.1)	3.56
8	12.2 (93.6)	9.60±0.03 (1.1)	11.60±0.03 (1.4)	14.10±0.05 (33.3)	7.80±0.05 (57.3)	3.15
9	15.2 (93.3)	10.16±0.03 (1.1)	12.25±0.03 (1.4)	14.70±0.04 (33.1)	8.14±0.04 (57.4)	3.30
10	11.4 (91.8)	9.72±0.03 (1.2)	11.58±0.03 (1.6)	13.97±0.05 (36.0)	7.62±0.05 (59.2)	3.14
11	14.0 (91.5)	11.24±0.03 (1.0)	13.48±0.03 (1.3)	15.74±0.05 (33.3)	8.34±0.05 (57.3)	3.54
12	16.2 (92.6)	10.04±0.03 (1.1)	11.75±0.03 (1.5)	13.26±0.04 (35.5)	6.92±0.04 (60.6)	3.02
13	15.0 (92.7)	12.42±0.03 (0.9)	14.44±0.03 (1.2)	15.93±0.05 (31.8)	7.72±0.04 (58.7)	3.58
14	24.2 (94.1)	11.30±0.02 (0.9)	12.89±0.02 (1.3)	13.12±0.03 (35.0)	6.04±0.03 (64.2)	3.03
15	14.1 (93.9)	14.22±0.03 (0.8)	15.84±0.03 (1.1)	15.40±0.05 (31.7)	6.88±0.04 (61.0)	3.63
16	6.2 (92.2)	11.44±0.04 (1.0)	13.02±0.05 (1.3)	13.56±0.07 (35.3)	6.51±0.07 (62.5)	3.14
17	14.2 (93.6)	8.81±0.03 (1.2)	10.41±0.03 (1.7)	12.08±0.04 (38.2)	6.45±0.04 (63.3)	2.73
18	18.6 (93.0)	9.17±0.02 (1.2)	10.98±0.02 (1.6)	12.93±0.04 (37.1)	7.16±0.04 (60.9)	2.93
19	12.9 (91.8)	7.20±0.02 (1.7)	8.62±0.03 (2.2)	10.29±0.05 (43.6)	5.72±0.05 (66.8)	2.33
20	16.8 (92.3)	7.08±0.02 (1.5)	8.49±0.02 (2.0)	10.08±0.04 (43.5)	5.64±0.04 (67.2)	2.28
21	17.4 (93.2)	12.26±0.03 (0.8)	14.91±0.03 (1.1)	17.56±0.04 (29.9)	9.42±0.04 (54.1)	3.93
22	10.5 (92.1)	10.36±0.03 (1.1)	12.25±0.03 (1.4)	14.25±0.05 (35.4)	7.77±0.05 (59.3)	3.24
23	12.1 (92.2)	10.29±0.03 (1.1)	12.34±0.03 (1.4)	14.71±0.05 (34.7)	8.00±0.05 (58.6)	3.30
24	16.4 (94.1)	10.08±0.02 (0.9)	12.07±0.03 (1.2)	14.48±0.04 (33.1)	8.05±0.04 (57.8)	3.26
25	3.2 (92.4)	15.57±0.07 (0.7)	18.56±0.08 (1.0)	21.20±0.11 (26.7)	10.95±0.10 (50.5)	4.76

* The deadtime-corrected exposures and the live-time fractions in percent in the parentheses.

† The NXB-subtracted count rates and the NXB fractions in percent in the parentheses. The errors are statistical errors only.

‡ The energy flux of 10–200 keV in an unit of $10^{-8} \text{ erg s}^{-1} \text{ cm}^{-2}$.